

Feedout and Richtmyer-Meshkov instability at large density difference

Alexander L. Velikovich and Andrew J. Schmitt

Plasma Physics Division, Naval Research Laboratory, Washington, D.C. 20375

John H. Gardner

LCP&FD, Naval Research Laboratory, Washington, D.C. 20375

Nathan Metzler

Physics Department, Nuclear Research Center Negev, P. O. Box 9001, Beer Sheva, Israel

Abstract

The feedout process transfers mass perturbations from the rear to the front surface of a driven target, producing the seed for the Rayleigh-Taylor (RT) instability growth. The feedout mechanism is investigated analytically and numerically for the case of perturbation wavelength comparable to or less than the shock-compressed target thickness. The lateral mass flow in the target leads to oscillations of the initial mass non-uniformity before the reflected rippled rarefaction wave breaks out, which may result in RT bubbles produced at locations where the areal mass was initially higher. This process is determined by the evolution of hydrodynamic perturbations in the rippled rarefaction wave, which is not the same as the Richtmyer-Meshkov (RM) interfacial instability. An exact analytical formula is derived for the time-dependent mass variation in a rippled rarefaction wave, and explicit estimates are given for the time of first phase reversal and frequency of the oscillations. The limiting transition from the case of RM perturbation growth at large density difference (low ambient density behind the rear surface) to the case of feedout (zero density) is studied, and it is shown that the latter limit is approached only if the ambient density is extremely low, less than 1/1000 of the pre-shock target density.

PACS numbers: 52.40.Nk, 52.35.Py

Report Documentation Page				Form Approved OMB No. 0704-0188	
Public reporting burden for the collection of information is estimated to average 1 hour per response, including the time for reviewing instructions, searching existing data sources, gathering and maintaining the data needed, and completing and reviewing the collection of information. Send comments regarding this burden estimate or any other aspect of this collection of information, including suggestions for reducing this burden, to Washington Headquarters Services, Directorate for Information Operations and Reports, 1215 Jefferson Davis Highway, Suite 1204, Arlington VA 22202-4302. Respondents should be aware that notwithstanding any other provision of law, no person shall be subject to a penalty for failing to comply with a collection of information if it does not display a currently valid OMB control number.					
1. REPORT DATE 2001		2. REPORT TYPE		3. DATES COVERED 00-00-2001 to 00-00-2001	
4. TITLE AND SUBTITLE Feedout and Richtmyer-Meshkov instability at large density difference				5a. CONTRACT NUMBER	
				5b. GRANT NUMBER	
				5c. PROGRAM ELEMENT NUMBER	
6. AUTHOR(S)				5d. PROJECT NUMBER	
				5e. TASK NUMBER	
				5f. WORK UNIT NUMBER	
7. PERFORMING ORGANIZATION NAME(S) AND ADDRESS(ES) Naval Research Laboratory, Plasma Physics Division, 4555 Overlook Avenue SW, Washington, DC, 20375				8. PERFORMING ORGANIZATION REPORT NUMBER	
9. SPONSORING/MONITORING AGENCY NAME(S) AND ADDRESS(ES)				10. SPONSOR/MONITOR'S ACRONYM(S)	
				11. SPONSOR/MONITOR'S REPORT NUMBER(S)	
12. DISTRIBUTION/AVAILABILITY STATEMENT Approved for public release; distribution unlimited					
13. SUPPLEMENTARY NOTES This article appeared in Physics of Plasmas and may be found at Phys. Plasmas 8, 592 (2001)					
14. ABSTRACT The feedout process transfers mass perturbations from the rear to the front surface of a driven target, producing the seed for the Rayleigh-Taylor (RT) instability growth. The feedout mechanism is investigated analytically and numerically for the case of perturbation wavelength comparable to or less than the shock-compressed target thickness. The lateral mass flow in the target leads to oscillations of the initial mass non-uniformity before the reflected rippled rarefaction wave breaks out, which may result in RT bubbles produced at locations where the areal mass was initially higher. This process is determined by the evolution of hydrodynamic perturbations in the rippled rarefaction wave, which is not the same as the Richtmyer-Meshkov (RM) interfacial instability. An exact analytical formula is derived for the time-dependent mass variation in a rippled rarefaction wave, and explicit estimates are given for the time of first phase reversal and frequency of the oscillations. The limiting transition from the case of RM perturbation growth at large density difference (low ambient density behind the rear surface) to the case of feedout (zero density) is studied, and it is shown that the latter limit is approached only if the ambient density is extremely low, less than 1/1000 of the pre-shock target density.					
15. SUBJECT TERMS					
16. SECURITY CLASSIFICATION OF:			17. LIMITATION OF ABSTRACT Same as Report (SAR)	18. NUMBER OF PAGES 54	19a. NAME OF RESPONSIBLE PERSON
a. REPORT unclassified	b. ABSTRACT unclassified	c. THIS PAGE unclassified			

I. INTRODUCTION

One of the sources that seed the initial mass perturbations for the Rayleigh-Taylor (RT) perturbation growth in laser fusion targets is the roughness of the inner surface of the target. The process that generates the RT mass perturbation seeds from the initial inner surface ripples is called feedout, see Refs. 1 to 3 and references therein. It should be noted that the first discussion and numerical simulation of the inner target surface roughness seeding the RT instability at its outer surface were presented in Ref. 4. In this paper, we neglect all other sources of non-uniformity (laser imprint, front surface roughness) and assume a constant pressure drive that may correspond either to a low-energy foot of the laser pulse or to a constant hohlraum temperature. Then for the single-mode, long-wavelength case^{1,3} defined in planar geometry by

$$\lambda \gg 2\pi L_s, \quad (1)$$

where λ is the perturbation wavelength, and L_s is the post-shock target thickness, the feedout could be visualized as shown in Fig. 1. A planar shock wave **S** approaches the rear surface ripples, first breaking out at the valleys, and then at the peaks [Fig. 1(a, b)]. A rippled rarefaction wave is reflected first from the valleys, then from the peaks. In the reference frame of the shocked mass, its leading edge **L** propagates at constant velocity a_1 , the speed of sound in the unperturbed shocked material. Therefore, the leading edge of the reflected rarefaction wave is a sine wave of the same phase as the initial rear surface ripple, and time-independent amplitude [Fig. 1(c)]. The shocked material expands into vacuum, starting from the valleys, at a constant velocity u_e , which for ideal gas equals $2a_1/(\gamma_1 - 1)$, so that after the sine-shaped expansion front **E** is fully formed, its ripple amplitude is also time-independent. The expansion front propagates faster than the

incident strong shock wave in the target, if $\gamma_1 < 2 + \sqrt{5} = 4.236$, in which case the phase of the expansion front is inverted with respect to the initial rear surface ripple [Fig. 1(c)]. Breakout of the rippled rarefaction wave occurs when its valleys (originated from the valleys at the rear surface of the target) reach the front surface [Fig. 1(c)], starting its acceleration. In other words, the thinner parts of the target start accelerating earlier, and experience a higher acceleration under the same driving pressure because of the lower areal mass. During the RT growth phase that follows, these thinner parts evolve into bubbles, propagating ahead and dumping more of their mass into the spikes that trail behind. This physical picture has been recently studied theoretically¹ and experimentally³.

In the present paper we study the case when the long-wavelength condition (1) does not hold. Then the situation changes in one important way: the lateral mass redistribution in the rippled rarefaction wave can no longer be neglected. The lateral mass flow is driven as shown in Fig. 1(b). After the shock breaks out, the expansion starts from the valleys, decreasing the pressure there, whereas near the peak locations the pressure is maintained at the constant post-shock value. The resulting lateral pressure gradient starts driving the mass from the peaks to the valleys, decreasing the pressure at the peaks and increasing it at the valleys. The mass flow continues when the pressure gradient vanishes, thus overshooting the equilibrium situation, and building up a reversed pressure gradient. These sonic oscillations of areal mass in a rippled rarefaction wave, which continue until the rarefaction wave breaks out at the front surface of the target, were first described in Ref. 5 (Fig. 14). In the context of the feedout problem, they were observed in the hohlraum-driven experiments on Nova and reproduced in the simulations.²

Feedout as described above is a hydrodynamic process that generates the actual seed for the RT instability starting from the ripples at the rear surface of the target. It should be emphasized that the feedout mechanism *per se* does not involve any interfacial hydrodynamic instability. There is no perturbation growth neither at the leading edge of the rippled rarefaction wave nor at the rippled expansion front. The density and pressure perturbations within the rippled rarefaction wave evolve as decaying sonic waves. Note, however, that the stable feedout situation could be regarded as a limiting case of a RM unstable flow, if we assume some low ambient density ρ_2 behind the rear surface of the target, and then let ρ_2 tend to zero. For any small but finite ρ_2 the rippled rarefaction wave is unstable,^{5, 6} and the RM instability growth, asymptotically linear in time, must take place at the contact interface between the decompressed target material and the shock-compressed ambient gas. Manifestation of the RM instability has been detected in the feedout simulations of Ref. 2. Do we have a contradiction here? To answer this question, it is important to study in detail the limiting transition $\rho_2 \rightarrow 0$ from the RM unstable to a stable feedout situation.

This paper is structured as follows. In Section II, we describe analytically the evolution of mass perturbations in a rippled rarefaction wave produced when a planar shock wave hits a rippled rear surface of the target, compare the results to the RM unstable situation when the half-space beyond the rear surface of the target is filled with a low-density gas, and study the limiting transition between the two cases. In Section III, we present simulation results for both cases and discuss the opportunities for their experimental verification, and Section IV concludes with a discussion.

II. THEORY

A. Formation of a rippled rarefaction wave

Consider a planar layer of ideal gas whose adiabatic exponent, initial density, and thickness are γ_1 , ρ_{01} , and L_0 , respectively. The half-space behind the layer $x > L_0$ contains a low-density gas with density ρ_2 and adiabatic exponent γ_2 . We are interested in the case of low ambient density $\rho_2 \ll \rho_{01}$ and in the limiting transition to the case of feedout, $\rho_2 = 0$. To exclude expansion of the layer into vacuum from behind prior to the shock arrival in the latter case, we neglect the initial pressure in both gases compared to the shock pressure. Then a constant pressure p_1 instantly applied to the front layer surface produces a strong shock wave whose velocity is

$$D_0 = \left[\frac{(\gamma_1 + 1)p_1}{2\rho_{01}} \right]^{1/2}. \quad (2)$$

Shock compression equals $(\gamma_1 + 1)/(\gamma_1 - 1)$. Density, x -velocity and speed of sound in the shocked gas are

$$\rho_1 = \frac{\gamma_1 + 1}{\gamma_1 - 1} \rho_{01}, \quad v_0 = \frac{2}{\gamma_1 + 1} D_0, \quad a_1 = \left(\frac{\gamma_1 p_1}{\rho_1} \right)^{1/2} = \frac{[2\gamma_1(\gamma_1 - 1)]^{1/2}}{\gamma_1 + 1} D_0, \quad (3)$$

respectively. By the end of the shock transit time interval, $t_s = L_0 / D_0$, the layer is compressed to its post-shock thickness, $L_s = (\gamma_1 - 1)L_0 / (\gamma_1 + 1)$.

At the instant of shock breakout, a centered rarefaction wave starts to propagate into the uniform shocked gas. Let us pass to the reference frame moving with the shocked gas and make $t = 0$ and $x = 0$ correspond to the time and place of the shock breakout, respectively. The gas flow in the centered rarefaction wave is self-similar:

$$A(x,t) \equiv \frac{a(x,t)}{a_1} = \frac{2}{\gamma_1 + 1} - \frac{\gamma_1 - 1}{\gamma_1 + 1} \frac{x}{a_1 t}, \quad (4)$$

$$\rho(x,t) = \rho_1 A(x,t)^{2/(\gamma_1-1)}, \quad p(x,t) = p_1 A(x,t)^{2\gamma_1/(\gamma_1-1)}, \quad (5)$$

where $a(x,t)$, $\rho(x,t)$ and $p(x,t)$ are local values of the sound velocity, density, and pressure, respectively. The strength of the rarefaction wave is characterized by the Mach number

$$M_1 = \frac{a_1^*}{a_1}, \quad (6)$$

where a_1^* is the speed of sound behind the rarefaction wave. The normalized speed of sound, $A(x,t)$, in a rarefaction wave varies between 1 at its leading edge and M_1 at its trailing edge. The values of density and pressure at the trailing edge are found by substituting $A = M_1$ into (5):

$$\rho_1^* = \rho_1 M_1^{2/(\gamma_1-1)}, \quad p_1^* = p_1 M_1^{2\gamma_1/(\gamma_1-1)}. \quad (7)$$

The Mach number M_1 varies between 1 and 0, the former value corresponding to a weak rarefaction (sound wave), and the latter — to a strong rarefaction (expansion into vacuum). In our case of strong shock-interface interaction, its value is found from

$$\frac{\rho_2}{\rho_{01}} = \frac{(\gamma_1 + 1)M_1^s}{(\gamma_2 + 1) \left[1 + s^{1/2}(1 - M_1) \right]^2}, \quad (8)$$

where $s = 2\gamma_1/(\gamma_1 - 1)$, see Refs. 5, 7. Inspection of Eq. (8) reveals that expansion into vacuum ($M_1 = 0$) corresponds to the feedout case $\rho_2 = 0$. However, a small value of the ratio ρ_2 / ρ_{01} does not necessarily imply that M_1 is also small because the power s could be large. Taking, for example, $\gamma_1 = \gamma_2 = 5/3$, so that $s = 5$, we find that density ratios

$\rho_2 / \rho_{01} = 10^{-1}, 10^{-2}, 10^{-3}$ and 10^{-4} would produce Mach numbers of the rarefaction wave $M_1 = 0.75, 0.53, 0.36$ and 0.24 , respectively. Note that the self-similar profiles (4), (5) do not depend on the rarefaction Mach number M_1 .

The leading edge of the rarefaction wave propagates in the negative x direction into the unperturbed resting uniform fluid at local sound velocity, a_1 : $x_l(t) = -a_1 t$. The rarefaction transit time equals

$$t_r = \frac{L_s}{a_1} = \left(\frac{\gamma_1 - 1}{2\gamma_1} \right)^{1/2} t_s \equiv \tilde{M}_0 t_s, \quad (9)$$

where \tilde{M}_0 is the Mach number characteristic of the shocked fluid flow with respect to the shock front. For an arbitrary equation of state, it must be $\tilde{M}_0 < 1$, so that the rarefaction transit time is always less than the shock transit time.

The trailing edge, which also propagates at local sound velocity a_1^* with respect to the fluid particles, separates the rarefaction wave from the uniform downstream flow, where density and pressure have constant values, ρ_1^* and p_1^* , and the fluid velocity equals

$$u_t = \frac{2a_1}{\gamma_1 - 1} (1 - M_1), \quad (10)$$

so that $x_t(t) = (u_t - M_1 a_1)t$. For expansion into vacuum, $M_1 = 0$, we have: $\rho_1^* = 0$,

$p_1^* = 0$, there is no gas behind the trailing edge, which in this case is called the expansion front. Its velocity equals $u_e = 2a_1 / (\gamma_1 - 1)$ and coincides with the fluid particle velocity (10).

Now introduce a small single-mode ripple at the rear surface of the layer.

Denoting the initial ripple amplitude by δx_0 , we find that immediately after the shock breakout the ripple amplitudes at the leading and trailing edges of the rarefaction wave are⁷

$$\delta x_l^* = \frac{1}{\gamma_1 + 1} \left\{ \gamma_1 - 1 + [2\gamma_1(\gamma_1 - 1)]^{1/2} \right\} \delta x_0, \quad (11)$$

$$\delta x_t^* = \frac{1}{\gamma_1 + 1} \left\{ \gamma_1 - 1 + \left(\frac{2\gamma_1}{\gamma_1 - 1} \right)^{1/2} [(\gamma_1 + 1)M_1 - 2] \right\} \delta x_0. \quad (12)$$

The leading edge ripple perturbation amplitude is time-independent, $\delta x_l(t) = \delta x_l^*$. The trailing edge perturbation amplitude grows linearly with time^{5, 6} for any nonzero M_1 . In the case of expansion into vacuum (feedout), it is also time-independent: $\delta x_t(t) = \delta x_t^*$.

B. Areal mass perturbations in a rippled rarefaction wave

A small-amplitude stability analysis of a rippled rarefaction wave has been done analytically, first in Ref. 8, and later, in a different way, in Ref. 5, and numerically, in Ref. 6. The results presented below are based on the analysis of Ref. 5, where the details could be found. Since the density is continuous at the edges of the rippled rarefaction wave, the contribution of the rippled rarefaction wave to the total areal mass perturbation (other contributions are discussed in Section IIIC) is given by

$$\begin{aligned} \delta m_r &= \int_{x_l(t)}^{x_t(t)} \delta \rho dx = \rho_1 \int_{x_l(t)}^{x_t(t)} A(x, t)^{2/(\gamma_1 - 1)} \frac{\delta \rho(x, t)}{\rho(x, t)} dx \\ &= \rho_1 \delta x_l^* \tau \frac{\gamma_1 + 1}{\gamma_1(\gamma_1 - 1)} \int_{M_1}^1 A^{2/(\gamma_1 - 1)} \Psi(A, \tau) dA. \end{aligned} \quad (13)$$

Here,

$$\tau = ka_1 t \quad (14)$$

is normalized time ($k = 2\pi / \lambda$ is the perturbation wave vector), $\delta\rho$ is the local density perturbation, $\Psi(A, \tau)$ is the relative pressure perturbation in the rarefaction wave normalized with respect to the constant value $k\delta x_l^*$, and A is related to x, t by (4). An explicit expression for $\Psi(A, \tau)$ is available for A close to 1:

$$\Psi(A, \tau) \cong \frac{2\gamma_1}{(\gamma_1 + 1)\tau} J_0 \left[\left(\frac{\gamma_1 + 1}{\gamma_1 - 1} \right)^{1/2} (1 - A)^{1/2} \tau \right], \quad (15)$$

where $J_0(z)$ is the Bessel function. In a general case,

$$\Psi(A, \tau) = \frac{1}{\tau} \sum_{j=0}^{\infty} \frac{\bar{\Psi}_j(A)}{j!} \left[\left(\frac{\gamma_1 + 1}{\gamma_1 - 1} \right) \frac{\tau^2}{4} \right]^j, \quad (16)$$

where calculation of the functions $\bar{\Psi}_j(A)$, $j = 0, 1, 2, \dots$, is described in Ref. 5. In particular,

$$\bar{\Psi}_0(A) = \frac{2\gamma_1(1 - \beta + \beta A)}{(\gamma_1 + 1)A}, \quad (17)$$

where, in our strong-shock approximation,

$$\beta = \frac{2\gamma_1(\gamma_1 + 1)}{2\gamma_1(\gamma_1 - 1) + (2\gamma_1)^{1/2}(\gamma_1 - 1)^{3/2}}. \quad (18)$$

In the limit $A \rightarrow 1$ this is consistent with (15), as it should be. With the help of (16)-(18), we find the initial value of areal mass perturbation characteristic of the rippled rarefaction wave:

$$\frac{\delta m_r(0)}{\rho_1 \delta x_l^*} = 1 - \frac{\gamma_1 - 1}{\gamma_1 + 1} \beta + M_1^{2/(\gamma_1 - 1)} \left(\beta - 1 - \frac{2\beta M_1}{\gamma_1 + 1} \right) \cong \begin{cases} 2 \frac{(1 - M_1)}{\gamma_1 - 1}, & M_1 \rightarrow 1, \\ 1 - \frac{\gamma_1 - 1}{\gamma_1 + 1} \beta, & M_1 \rightarrow 0. \end{cases} \quad (19)$$

Substituting (16) into (13), we obtain a general expression for the mass perturbation in the rippled rarefaction wave:

$$\delta m_r(\tau) = \rho_1 \delta x_l^* \frac{(\gamma_1 + 1)}{\gamma_1(\gamma_1 - 1)} \sum_{j=0}^{\infty} \frac{1}{j!} \left[\left(\frac{\gamma_1 + 1}{\gamma_1 - 1} \right) \frac{\tau^2}{4} \right]^j \int_{M_1}^1 A^{2/(\gamma_1 - 1)} \overline{\Psi}_j(A) dA. \quad (20)$$

This expression could be simplified for the limiting cases of weak and strong rarefaction waves. In the former case, $1 - M_1 \ll 1$, an explicit approximate formula for $\delta m_r(\tau)$ is derived by substituting (15) into (13):

$$\delta m_r(\tau) \cong \rho_1 \delta x_l^* \frac{4}{\tau} \left(\frac{1 - M_1}{\gamma_1^2 - 1} \right)^{1/2} J_1 \left[\left(\frac{\gamma_1 + 1}{\gamma_1 - 1} \right)^{1/2} (1 - M_1)^{1/2} \tau \right]. \quad (21)$$

A weak reflected rarefaction wave could be produced in our case of a strong shock-interface interaction if the density ratio ρ_2 / ρ_{01} were a little less than the total transmission value $(\gamma_1 + 1)/(\gamma_2 + 1)$ found by substituting $M_1 = 1$ into (8). (Alternatively, the density ratio could be much smaller than this value, but then the incident shock wave should be weak.) For instance, assuming $\gamma_1 = \gamma_2 = 5/3$ and $\rho_2 / \rho_{01} = 0.95$, we find from (8): $M_1 = 0.9946$. Figure 2 shows the time history of areal mass perturbation calculated analytically for this case. The solid and dotted lines correspond to the exact solution (20) and to the approximation (21), respectively, in good agreement with each other. The oscillations are standing sonic waves excited in the rarefaction wave by the lateral pressure gradient, which drives the gas from the high to the low pressure/density areas. The lateral mass flow continues when the pressure gradient vanishes, thus overshooting the equilibrium situation, but not by much: as seen in Fig. 2, the peak value of mass perturbation amplitude with inverted phase is only 13% of its initial value. At late time, the oscillation amplitude decays as $\tau^{-3/2}$, see Eq. (21).

For the case of feedout (strong rarefaction wave, $M_1 = 0$), the integrals in Eq. (20) are evaluated explicitly, without calculating the functions $\overline{\Psi}_j(A)$. This is done by multiplying Eqs. (63), (64) of Ref. 4, which determine these functions, by $A^{2/(\gamma_1-1)}$, integrating them over A from 0 to 1, and using the boundary conditions (66). Then, after some algebra, we obtain:

$$\delta m_r(\tau) = \rho_{01} \delta x_0 \cdot \frac{2(3-\gamma_1)(\gamma_1+1)}{\gamma_1+1-(\gamma_1-1)\beta} \sum_{j=0}^{\infty} \frac{(-1)^j}{j!} \left[\left(\frac{\gamma_1+1}{3-\gamma_1} \right) \frac{\tau^2}{4} \right]^j \frac{\Gamma \left[\frac{2(\gamma_1-1)}{3-\gamma_1} j + \frac{3}{2} \right]}{\Gamma \left[\frac{\gamma_1+1}{3-\gamma_1} j + \frac{1}{2} \right]} \quad (22)$$

$$\times \frac{[(\gamma_1-1)(2j-\beta) + \gamma_1+1]}{[(\gamma_1-1)j+1] \{4[(\gamma_1-1)j+1]^2 - (\gamma_1-1)^2\}},$$

where $\Gamma(z)$ is the Euler gamma function. Note that this expression is exact, not approximate, like (21), and its right-hand side is finite at $\gamma_1 = 3$. Equation (19) was used to normalize the areal mass perturbation amplitude with respect to its initial value, which, of course, is the same as the rear surface mass non-uniformity of the target prior to the shock breakout: $\delta m_r(0) = \rho_{01} \delta x_0$.

The infinite series (22) converges at all times and represents an entire analytic function of complex time τ . At early time, this function could be approximated by the first two terms of the series:

$$\delta m_r(\tau) \cong \rho_{01} \delta x_0 \left(1 - \frac{\tau^2}{\tau_1^2} \right) \quad \text{at} \quad \tau \leq \tau_1, \quad (23)$$

where the coefficient

$$\tau_1 = \left\{ \frac{2\gamma_1(3\gamma_1-1)[\gamma_1+1-(\gamma_1-1)\beta]}{(\gamma_1+1)[3\gamma_1-1-(\gamma_1-1)\beta]} \right\}^{1/2} \quad (24)$$

could be regarded as the first-order estimate of the time interval between the shock breakout and the first phase reversal of areal mass perturbation.

At $|\tau| \rightarrow \infty$, the function generated by the series (22) has an essential singularity, like exponential or Bessel functions. The main exponential term describing its divergence near this singularity, at $\tau \rightarrow \pm i\infty$, is immediately found by simplifying the expression for the series coefficients at large j : $\delta m_r \cong \text{const} \cdot \sinh(\Omega\tau)/(\Omega\tau)$, where the values of *const* and Ω are given below. On the real axis, the corresponding terms become oscillatory, describing the most rapidly varying part of the solution:

$$\delta m_r(\tau) \cong \rho_{01} \delta x_0 \cdot \frac{4\sqrt{2}(\gamma_1 + 1)}{(\gamma_1 - 1)[\gamma_1 + 1 - (\gamma_1 - 1)\beta]} \cdot \frac{\sin(\Omega\tau)}{\Omega\tau} + (...), \quad (25)$$

where () stands for the terms slowly varying in comparison with $\sin(\Omega\tau)/(\Omega\tau)$,

$$\Omega = \left[\frac{2(\gamma_1 - 1)}{\gamma_1 + 1} \right]^{(\gamma_1 - 1)/(3 - \gamma_1)} \quad (26)$$

is a function of γ_1 that decreases from 1 at $\gamma_1 \rightarrow 1$ to 1/2 at $\gamma_1 \rightarrow \infty$. In particular,

$$\Omega(\gamma_1 = 5/3) = 1/\sqrt{2} = 0.707 \quad \text{and} \quad \Omega(\gamma_1 = 3) = 1/\sqrt{e} = 0.607.$$

Figure 3 demonstrates oscillations of areal mass calculated using (22) for strong rarefaction waves ($M_1 = 0$, expansion into vacuum), which emerge in the feedout process. The first term in the right-hand side of Eq. (25) turns out to be a good approximation to the late-time behavior of δm_r for $1 < \gamma_1 < 2$. In Fig. 3(a), we compare the exact solution (22) for $\gamma_1 = 5/3$ (solid line) to the asymptotic term (25) (dotted line), demonstrating a good agreement after $\tau \sim 15$. Figure 3(b) compares the exact results for different values of γ_1 between 1 and 2. Overshooting of the initial amplitude is found to

be large for all cases: by a factor ranging from 2.5 to 3.3 for γ_1 varied between 7/5 and 9/5. One or two of the following peaks are even higher. Figure 3(c) demonstrates a different behavior found for higher γ s. The amplitude is shifted to negative values and exhibits a slow (not faster than linear) growth, which becomes more pronounced as γ is increased. This could indicate some weak instability of a rippled rarefaction wave that takes place even at $M_1 = 0$, is visible mostly at high γ s, and has not been noticed before.^{5,6} Note that the oscillating contributions to the exact solutions shown in Fig. 3(c) are well approximated by Eq. (25).

The time of first phase reversal is in good agreement with the estimate (24), the error in all cases being 4% to 5%. In agreement with (26), frequency of oscillations slightly decreases with increased γ_1 . At late time, the oscillation amplitude decays as τ^{-1} , as predicted by Eq. (25). The time interval between the first and the second phase reversals scales as $1/\Omega$:

$$\Delta\tau_1 = \frac{\pi}{\Omega}\theta(\gamma_1), \quad (27)$$

where $\theta(\gamma_1)$ is a dimensionless correction factor of order unity. This factor tends to unity in the limit $\gamma_1 \rightarrow 1$. Its values for $\gamma_1 = 7/5$, $5/3$, $9/5$, 2 , $8/3$, and 2.82 are 1.04, 1.19, 1.26, 1.36, 1.77, and 2.03, respectively. As seen in Fig. 3(c), for $\gamma_1 > 2.82$, no second phase reversal is predicted.

Figure 4 shows how the mass perturbation behavior changes as its Mach number is gradually increased from 0 to 0.8 ($\gamma_1 = \gamma_2 = 5/3$). As found from (8), the values of $M_1 = 0.2, 0.4, 0.6$, and 0.8 correspond to the ratios $\rho_2 / \rho_{01} = 4.1 \times 10^{-5}, 1.9 \times 10^{-3}, 2.2 \times 10^{-2}$, and 0.16 , respectively. To facilitate the comparison, the mass perturbation amplitudes are

also normalized here to the respective values of $\delta m_r(0)$ given by (19). We see that the amplitude of the first inverted peak is very sensitive to the density ratio. E. g., addition of a very small ambient density $\rho_2 / \rho_{01} = 1.9 \times 10^{-3}$ behind the rear surface results in a significant (27%) reduction of the relative amplitude of the negative peak compared to the case of feedout (expansion into vacuum).

This theory of feedout applies until the rarefaction wave breaks out at the front surface. From (9) and (14), we find that this instant corresponds to $\tau = \tau_r$ defined as

$$\tau_r = k a_1 t_r = k L_s = \frac{2\pi L_s}{\lambda}, \quad (28)$$

cf. Eq. (1). If $\tau_r > \tau_1$, then our feedout experiment or simulation must show a phase reversal of mass perturbation in a rippled rarefaction wave. If $\tau_r > \tau_1 + \pi\theta / 2\Omega$, then we should also observe the first inverted peak. For the experiments of Ref. 3 (plastic, $L_0 = 25 \mu\text{m}$, $\lambda = 100 \mu\text{m}$), assuming a (2.5 to 3)-fold shock compression of plastic, we find: $\tau_r = 0.52$ to 0.63 . The estimate (24) demonstrates that this is definitely insufficient for phase inversion: in the range of γ_1 from 1 to 2.5 the value of τ_1 varies between 1.25 and 1.64. As found from (23), the above value of τ_r corresponds only to a ~15 to 20% reduction in the mass variation amplitude by the time of the rarefaction wave breakout in comparison with the long-wavelength limit $\tau_r \rightarrow 0$. Thus the long-wavelength assumption (1) is valid in the case of this experiment, and the theory of Ref. 1 applies. This is not the case for the thick-foil experiment of Ref. 2, where the initial thickness of an aluminum slab was $L_0 = 86 \mu\text{m}$, and the rear side ripple wavelength $\lambda = 50 \mu\text{m}$. A 3-fold shock compression of solid aluminum would correspond to $\tau_r = 3.6$, which exceeds

τ_1 for any reasonable value of γ_1 . In particular, for $\gamma_1 = 5/3$ we have:

$\tau_1 + \pi\theta / 2\Omega = 4.0$. As demonstrated by Eq. (24) and our Fig. 3, the value of $\tau_r = 3.6$ is large enough for phase inversion and agrees with a ~ 2.5 -fold excess of mass variation with inverted phase over its initial value, which is shown in Fig. 7 of Ref. 2.

C. RM instability at large density difference

We have demonstrated above that the feedout process does not involve any interfacial hydrodynamic instability. Nevertheless, the vorticity-driven RM perturbation growth at the rear surface has been discussed in connection with feedout in Refs. 2, 3. To find out if there is any contradiction here, let us assume, as done in most computational studies that use Eulerian or Lagrangian-Eulerian codes, that there is some low-density ambient gas behind the rear surface of our gas layer, and consider the limiting transition from the low-density case $\rho_2 / \rho_{01} \ll 1$ to the feedout case of $\rho_2 = 0$. In the former case, the RM instability would inevitably develop for any ρ_2 / ρ_{01} , no matter how small, whereas the latter case is essentially stable. Obviously, we must obtain the same results for evolution of mass perturbations in the stable case $\rho_2 = 0$ and in the limiting transition $\rho_2 / \rho_{01} \rightarrow 0$ from an essentially RM unstable situation. The questions are: How small should the ratio ρ_2 / ρ_{01} be in order to make all the contributions to areal mass variation, other than the rippled rarefaction wave, negligible? How does the RM instability develop when its contribution to the mass variation is no longer significant?

The shock-interface interaction makes the contact interface move in positive x -direction at the velocity u_i given by (10) and produces a strong transmitted shock wave

propagating into the ambient gas at the velocity $D_2 = (\gamma_2 + 1)u_t / 2$. Now the contact interface separates ambient gas, shock-compressed to the density

$$\rho_2^* = \frac{\gamma_2 + 1}{\gamma_2 - 1} \rho_2, \quad (29)$$

and the expanded rear surface of our layer, where the gas density is given by (7). From (7), (8) and (29) we find the post-interaction density ratio at the contact interface:

$$\frac{\rho_2^*}{\rho_1^*} = \frac{(\gamma_1 - 1)M_1^2}{(\gamma_2 - 1)[1 + s^{1/2}(1 - M_1)]^2} \cong \frac{(\gamma_1 - 1)}{(\gamma_2 - 1)(1 + s^{1/2})^{2/\gamma_1}} \left[\frac{(\gamma_2 + 1)\rho_2}{(\gamma_1 + 1)\rho_{01}} \right]^{(\gamma_1 - 1)/\gamma_1} \quad (30)$$

in the limit $\rho_2 / \rho_{01} \rightarrow 0$. The density contrast at the interface therefore remains high in this limit, although the densities at both sides of the interface tend to zero. At $\rho_2 = 0$, the contact interface coincides with the trailing edge of the rarefaction wave, the expansion front, see (10).

The total mass variation produced in the RM unstable flow could be presented as

$$\delta m(\tau) = \delta m_r(\tau) + \delta m_{se}(\tau) + \delta m_c(\tau) + \delta m_s(\tau). \quad (31)$$

Here, $\delta m_r(\tau)$ is the mass variation in the reflected rarefaction wave given by (20);

$\delta m_{se}(\tau)$ is the contribution due to sonic and entropy perturbations in the uniform flow regions on both sides of the contact interface,

$$\delta m_{se}(\tau) = \int_{x_t}^{x_s} \delta \rho(x, \tau) dx, \quad (32)$$

[where $\delta \rho(x, \tau)$ is the local density perturbation, and $x_s = D_2 t$ is the coordinate of the transmitted shock front], $\delta m_c(\tau)$ and $\delta m_s(\tau)$ are contributions of the perturbations at the contact interface and transmitted shock front, respectively:

$$\delta m_c(\tau) = (\rho_1^* - \rho_2^*) \delta x_c(\tau), \quad \delta m_s(\tau) = (\rho_2^* - \rho_2) \delta x_s(\tau), \quad (33)$$

[where $\delta x_c(\tau)$ and $\delta x_s(\tau)$ are the displacement amplitudes of the contact interface and transmitted shock front, respectively]. We calculate the time-dependent perturbation amplitudes $\delta \rho(x, \tau)$, $\delta x_c(\tau)$, and $\delta x_s(\tau)$, and evaluate $\delta m(\tau)$ analytically following the procedures of Refs. 7, 9, and using Eq. (20). The results shown in Figs. 5(a) to (d) refer to $\gamma_1 = \gamma_2 = 5/3$ and $\rho_2 / \rho_{01} = 10^{-1}$, 10^{-2} , 10^{-3} and 10^{-4} . We plot the total mass variation (31) and the contributions to it due to rippled rarefaction wave, $\delta m_r(\tau)$ (which should dominate in the feedout limit) and to the rippled contact interface, $\delta m_c(\tau)$ (this one dominates at late times in the RM-unstable situation).

For $\rho_2 / \rho_{01} = 10^{-1}$ [Fig. 5(a)] the linearly growing interfacial contribution $\delta m_c(\tau)$ to the total mass variation is dominant, whereas the lateral mass transfer in the rippled rarefaction wave adds some oscillatory correction. For $\rho_2 / \rho_{01} = 10^{-2}$ [Fig. 5(b)], contribution of the oscillations is much larger, but the linearly growing term $\delta m_c(\tau)$ still prevails in determining the evolution. At $\rho_2 / \rho_{01} = 10^{-3}$ [Fig. 5(c)], the contribution of the rippled rarefaction wave characteristic of the feedout is dominant, although the correction due to the interfacial term is not so small — about 10% at the first inverted peak. Finally, at $\rho_2 / \rho_{01} = 10^{-4}$ [Fig. 5(d)] the contribution of the rippled rarefaction wave prevails. We come to the conclusion that an accurate numerical modeling of the feedout process requires the ambient density (which is not there in the feedout experiments, and is typically introduced in simulations to make the codes work) to be less than 10^{-3} . Otherwise the simulation results could contain a numerical artifact — that is, a significant contribution from the contact interface which is not really there.

We have seen that in the limit $\rho_2 / \rho_{01} \rightarrow 0$ the contribution of the contact interface to the total mass variation becomes small. Its smallness, however, comes from the small density factor $\rho_1^* - \rho_2^*$ in Eq. (33). It does not imply that the interface displacement, $\delta x_c(\tau)$, should also be small. In fact, $\delta x_c(\tau)$ typically exceeds the initial value, δx_0 , by a large factor, growing with time as it should in the RM unstable situation. This perturbation development, as we demonstrate below, is somewhat unusual due to the low value of ρ_2 / ρ_{01} . Besides, in the low-density limit we can expect a freeze-out¹⁰, which means zero asymptotic value of the RM interfacial growth rate. For our case of reflected rarefaction wave, the latter could be estimated with the aid of the so-called prescriptions due to either Meyer and Blewett (MB)¹¹ or Vandenboomaerde *et al.* (VMG)¹²:

$$\Gamma_\infty = \lim_{t \rightarrow \infty} \frac{d}{dt} \delta x_c(t) = \begin{cases} ku_t \times \frac{1}{2} A^* (\delta x_0 + \delta x_c^*) & \text{(MB),} \\ ku_t \times \frac{1}{2} (A \delta x_0 + A^* \delta x_c^*) & \text{(VMG),} \end{cases} \quad (34)$$

where the pre- and post-interaction Atwood numbers are defined as

$A = (\rho_2 - \rho_{01}) / (\rho_2 + \rho_{01})$ and $A^* = (\rho_2^* - \rho_1^*) / ((\rho_2^* + \rho_1^*))$, respectively, and δx_c^* is the post-interaction interface ripple amplitude, which in our strong-shock case equals to

$$\delta x_c^* = \frac{1}{\gamma_1 + 1} \left\{ \gamma_1 - 1 - 2(1 - M_1) \left(\frac{2\gamma_1}{\gamma_1 - 1} \right)^{1/2} \right\} \delta x_0 \quad (35)$$

[at $M_1 = 0$, the contact interface coincides with the expansion front, so that the displacement amplitudes (35) and (12) are identical, as they should be.] In the limit $\rho_2 / \rho_{01} \rightarrow 0$ both $A \rightarrow -1$ and $A^* \rightarrow -1$, so both prescriptions predict nearly the same

asymptotic growth rate. The freeze-out, $\Gamma_\infty = 0$, is predicted for the case when the shock-interface interaction inverts the phase of the interface ripple without affecting its amplitude, $\delta x_c^* = -\delta x_0$. The corresponding density ratio is found from (8), (34), (35):

$$\left(\frac{\rho_2}{\rho_{01}} \right)_{\text{freeze-out}} = \frac{1}{(\gamma_1 + 1)(\gamma_2 + 1)} \left\{ 1 - \left[\frac{\gamma_1(\gamma_1 - 1)}{2} \right]^{1/2} \right\}^{2\gamma_1/(\gamma_1 - 1)}. \quad (36)$$

The RM freeze-out at low ambient densities could therefore be expected for $\gamma_1 < 2$.

Taking $\gamma_1 = \gamma_2 = 5/3$, we find: $(\rho_2 / \rho_{01})_{\text{freeze-out}} = 1.5 \cdot 10^{-4}$.

Figure 6(a) demonstrates the time history of a classical RM growth at $\gamma_1 = \gamma_2 = 5/3$, $\rho_2 / \rho_{01} = 10^{-3}$. Here, displacement of the contact interface δx_c is shown in units of δx_0 , and the normalized growth rate (or, which is the same, the x -velocity perturbation amplitude at the interface) δv_c - in units of $ku_i \delta x_0$. Recall that typically, the time-dependent RM growth rate approaches its constant asymptotic value quite fast [in our present units (14), by $\tau = 15$ to 20], and then stays near it, slightly oscillating, see Refs. 7, 13, and references therein. Here, the convergence to the asymptotic value apparently takes much longer — on the time scale of Fig. 6 we do not see it yet. The oscillatory behavior of the growth rate, with two distinct frequencies that correspond to lateral sonic waves in two fluids separated by the interface, is characteristic of the low ambient density case. Still, the growth rate remains negative, and we observe an approximately linear growth of δx_c with some superimposed oscillations.

Figure 6(b) represents the same for the case $\rho_2 / \rho_{01} = 1.5 \cdot 10^{-4}$. Here, the MB prescription for the asymptotic growth rate predicts a freeze-out, whereas the VMG prediction is slightly negative. Indeed, the growth rate that is initially negative, changes

sign at $\tau = 11.2$, and the perturbation amplitude reaches its peak value and begins to decrease. Note that our analytic calculation has not converged to the asymptotic growth rate (which must be zero in the case of freeze-out). Nevertheless, comparing Figs. 6(a) and (b), we see the growth rate shifted from negative to positive values with decreased ratio ρ_2/ρ_{01} , so that prediction of the freeze-out seems to make sense. The evolution of perturbations for the exact (that is, determined from compressible linear theory rather than the MB or VMG prescriptions) value of $(\rho_2/\rho_{01})_{\text{freeze-out}}$ at $\tau < 20$ should not differ much from that shown in Fig. 6(b). Note, that a standard-looking RM growth in the negative direction that could have been revealed by a simulation carried out for the conditions of Fig. 6(b) up to, say, $\tau = 10$, might be totally misleading — in effect, this is not a real growth but rather just one phase of decaying oscillations, that should approach, at very large τ , some constant value of δx_c .

III. NUMERICAL SIMULATION

Now we compare our analytical results to numerical simulations. The comparison serves two purposes. First, we do the comparison for a somewhat idealized case of a constant intensity shock wave driven by external pressure into a uniform gas layer with ripples at the rear surface. Here, the exact analytical results are used to test the accuracy of our code in the feedout-related problems. Second, we simulate the feedout produced in a laser-driven planar plastic target. In this case, the roles are reversed, and the code is used to test whether the predictions based on an idealized analytical model hold in a realistic feedout situation.

Our simulations were performed in two dimensions (2D) using the FAST2D hydrocode developed at the Naval Research Laboratory¹⁴ (more details and further

references are given in Refs. 9, 15). We begin with a test case of classical RM instability developing at an interface between two ideal gases with $\gamma_1 = \gamma_2 = 5/3$ and different densities. The initial conditions correspond to the instant when a shock front hits the valleys of the rippled interface. The pre-shock density is $\rho_{01} = 1 \text{ g/cm}^3$, the post-shock pressure is $p_1 = 1 \text{ Mbar}$, exceeding the pre-shock pressure by a factor of 1000. Then the planar shock velocity is $D_0 = 1.15 \cdot 10^6 \text{ cm/s}$, the post-shock density and speed of sound are $\rho_1 = 4 \text{ g/cm}^3$ and $a_1 = 6.45 \cdot 10^5 \text{ cm/s}$, respectively, as given by Eqs. (1), (2) and reproduced in the simulation. The wavelength of the interfacial perturbation is $\lambda = 50 \text{ }\mu\text{m}$, and the initial amplitude $\delta x_0 = 0.5 \text{ }\mu\text{m}$, satisfying the linearity condition ($k\delta x_0 = 0.063$). The time of shock-interface interaction is $\Delta t_0 = 2\delta x_0 / D_0 = 0.09 \text{ ns}$.

Figure 7 compares the analytical and numerical time evolution of areal mass perturbation for a conventional classical RM case of $\rho_2 / \rho_{01} = 10^{-1}$ corresponding to Fig. 5(a). We see a reasonably good agreement, particularly in the times when phase reversal, minimum and maximum of the mass perturbation amplitude occur (note the early-time shift between the two curves by about Δt_0). The difference between the two curves should be attributed to numerical diffusion rather than to a non-linearity (even near the peak amplitude, $k\delta x_c$ does not exceed 0.25).

Figure 8 corresponds to the case $\rho_2 / \rho_{01} = 10^{-3}$ [Fig. 5(c)]. This could be regarded as a simulation of a RM instability at large density difference, or, alternatively, as a simulation of feedout. From the latter point of view, the above small density ratio is simply an inescapable numerical approximation to the actual (zero) value. Dotted and dashed curves in Fig. 8 are theoretical predictions for $\rho_2 = 0$ and $\rho_2 / \rho_{01} = 10^{-3}$,

respectively, indeed quite close to each other. The time of first phase reversal, t_1 , and the time interval between the first and second phase reversals, Δt_1 , could be compared to the estimates (24) and (26), (27):

$$t_1 = \frac{\lambda}{2\pi a_1} \tau_1, \quad \Delta t_1 = \frac{\lambda}{2\Omega a_1} \theta(5/3). \quad (37)$$

For $\gamma_1 = 5/3$ we have: $\tau_1 = (5 - \sqrt{5})/2$, $\Omega = 1/\sqrt{2}$, $\theta = 1.19$, so $t_1 = 1.7$ ns, $\Delta t_1 = 6.5$ ns, again, in a good agreement with the simulation. The peak perturbation amplitude is reproduced in the simulation less accurately than in Fig. 7. This appears to be due to greater influence of numerical diffusion at large density difference.

Now consider a 60 μm thick solid plastic target with ripples at the rear surface separating it from a gas or foam whose initial density ρ_2 is varied from ρ_0 to $3\rho_0$ of the solid plastic density, $\rho_0 = 1.07$ g/cm³. We simulate irradiation of this target with a uniform 0.248 nm KrF laser beam, as in Nike laser at the Naval Research Laboratory¹⁶. The code in this simulation includes inverse bremsstrahlung laser energy absorption (multiple ray trace), Spitzer-Harm thermal conduction, and tabulated equation of state (EOS) of plastic. Radiation energy transport, which is also included in the code, has not been invoked here, since we are mostly interested in evolution of mass perturbations in the bulk of the target, where the radiation does not reach. We are not attempting to describe in any detail the subsequent RT growth, which could be significantly affected by the radiation transport.

Figure 9 shows the results obtained for the beam intensity, which increases linearly from 1.8×10^{13} W/cm² to 3×10^{13} W/cm² in 6 ns, and then stays constant (this corresponds to an almost constant driving pressure $p_1 \cong 0.8$ Mbar), initial rear surface

ripple amplitude $\delta x_0 = 1 \mu\text{m}$ and wavelength $\lambda = 15 \mu\text{m}$. The planar shock wave propagates at the speed $D_0 = 1.14 \cdot 10^6 \text{ cm/s}$, compresses solid plastic by a factor of 2.2, and breaks out at the valleys of the rippled rear surface at 5.1 ns. The shock-ripple interaction takes $\Delta t_0 = 2\delta x_0 / D_0 = 0.18 \text{ ns}$, the evolution described in Section IIB thus starting about 5.3 ns. The sound velocity in shock-compressed plasma is $a_1 = 1.14 \cdot 10^6$, so that the rarefaction transit time is 2.3 ns, and the acceleration phase starts at about 7.4 ns.

To check our analytical estimates, we have to select some effective value of γ_1 approximating the realistic EOS of plastic. One can do it, for instance, estimating γ_1 from the compression ratio: according to Eq. (3), a 2.2-fold shock compression corresponds to $\gamma_1 = 8/3$. Then, in the feedout limit $\rho_2 \rightarrow 0$, according to Eq. (37) (where $\gamma_1 = 8/3$ corresponds to $\tau_1 = 1.7$, $\Omega = 0.62$, $\theta = 1.77$) we obtain: $t_1 = 0.36 \text{ ns}$, $\Delta t_1 = 1.9 \text{ ns}$. In other words, the first phase reversal is predicted at 5.6 ns, and the second — at 7.5 ns, which is in good agreement with the results shown in Fig. 9. We see that for $\rho_2 / \rho_{01} < 10^{-1}$ the overshooting of the initial areal mass perturbation amplitude in first phase-reversed peak is about 3-fold, again in agreement with the theory of Section IIB.

At late time, $t \rightarrow \infty$ the pressure p_1 would drive the shocked mass into the half-space filled by the gas of density ρ_2 at some constant speed v_2 , which is found from (2)-(3), where ρ_{01} and v_0 should be replaced by ρ_2 and v_2 , respectively. The transient regime of accelerated motion lasts about $(\rho_{01} / \rho_2)^{1/2} t_s$. Therefore, evolution of mass variation after the rarefaction breakout is determined by a complicated interplay of the

RM instability at the contact interface, and RT and RM-like¹⁷ instabilities at the ablation front. This rather complex behavior is observed in Figure 9.

In direct-drive laser fusion, a constant low-energy foot of the laser pulse, which provides the desired value of the target's adiabat during the first shock compression, is typically followed by a main drive pulse of much higher intensity. Most of the target acceleration and RT perturbation growth occur during the main pulse. However, the seeds for the RT growth, which in our case come from the rear-surface ripple, are largely generated earlier. The oscillatory early-time evolution of perturbations makes the subsequent RT growth phase-sensitive: a RT bubble can develop where the target was initially thinner or thicker, depending on the perturbation wavelength, target thickness and the laser beam parameters.

This is illustrated by Fig. 10. Figure 10(a) shows the laser pulse shape, with rapid intensity increase from the foot to the main drive level at about 5.8 ns. The background gas density is taken $10^{-3} \times \rho_{01}$. In Fig. 10(b), the evolution of mass perturbation amplitudes is presented for several ripple wavelengths. As expected [see (36)], the time interval between the shock breakout and the first phase reversal is proportional to the perturbation wavelength λ . Shortly after this, the RT instability starts to develop, which means that the thickness of compressed target L_s becomes a significant scale, comparable to the perturbation wavelength (in our example, $L_s \approx 25 \text{ } \mu\text{m}$). Indeed, we observe a quite complicated behavior rather than self-similar. In particular, the exponential RT growth occurs with initial perturbation phase (albeit after two phase reversals) for $\lambda = 40 \text{ } \mu\text{m}$, and with inverted phase for $\lambda = 30 \text{ } \mu\text{m}$. In other words, for

$\lambda = 40 \text{ } \mu\text{m}$ the RT bubble develops where the target was initially thinner, and for $\lambda = 30 \text{ } \mu\text{m}$ - where it was initially thicker.

Figure 11 illustrates the latter case with the density maps shown at $t = 0, 6.9, 8.4,$ and 9.6 ns . Note the first phase reversal at the rear surface on Fig. 11(b), similar to that shown in Fig. 1(c). Then the laser intensity increase to the main drive level produces the second shock wave, and by the time the second rarefaction wave breaks out at the front surface, the rear surface changes its phase again [Fig. 11(c)]. Although the total mass perturbation at that time has the same phase as the original rear-surface perturbation [Fig. 11(a)], the RT instability starts to develop at the front surface, where the mass perturbation has the opposite sign, and maintains this phase throughout its exponential growth. The 3 total phase changes of mass perturbation observed in Fig. 10 occur because the rear interface changes phase again and its contribution to the total mass perturbation remains dominant before the RT eigenmode (with the opposite sign) takes over. The net result is that the bubbles develop where the target is initially thicker, in contrast with what would be expected in the long-wavelength limit,^{1,3} and is actually seen in our case of $\lambda = 85 \text{ } \mu\text{m}$, when there is not enough time even for a single phase reversal (or, to be more precise, when the phase reversal occurring near the rear surface is more than compensated by the RT growth starting near the front surface at the initial perturbation phase.) Comparing the $\lambda = 30 \text{ } \mu\text{m}$ case to the others, we note that the two phase reversals seen in Fig. 10 for $\lambda = 40 \text{ } \mu\text{m}$ occur because the second shock reaches the rear surface before the mass perturbation there changes sign.

The complicated behavior of mass perturbations due to feedout, as described above, has yet to be studied in the experiments. So far, the indirect-drive experiment²

demonstrated a complete phase reversal, whereas in the direct-drive experiment³ the onset of an areal-mass oscillation at the fundamental harmonic is clearly seen on their Fig. 4. To advance from there, one needs to do a careful design of an experiment under a number of constraints. 1) In order to observe more of the oscillations, it is desirable to have a longer driving laser pulse than those of Refs. 2, 3 (about 2.2 ns). 2) The laser drive should be sufficiently uniform, to prevent the target from being torn apart by the short-wavelength laser-imprinted perturbations while we try to follow the perturbation development at the fundamental harmonic of the rear surface ripple. 3) To increase the frequency of oscillations, it is preferable to deal with short ripple wavelength in the range 15 to 30 μm (although by varying the pulse duration and intensity and target thickness, one could probably use longer wavelengths), which is quite a challenge for the imaging diagnostics. In our opinion, the Nike laser facility¹⁶ at the Naval Research Laboratory (NRL), with its long pulses (4 ns standard could be extended to 8 ns) and low beam non-uniformity (0.25%) is clearly the best laser driver for such an experiment. The monochromatic x-ray imaging diagnostic technique developed and fielded on Nike¹⁸ provides sufficient spatial resolution to observe peak-to-valley mass variation above 2 μm of solid plastic at the wavelengths greater than 15 μm . Design of a Nike feedout experiment is now in progress.

IV. CONCLUSIONS

We have studied the feedout mechanism that generates the seed for the RT instability starting from the ripples at the rear surface of the target through hydrodynamic evolution of mass perturbations in a rippled reflected rarefaction wave. We have shown

that the feedout represents a quite special (stable) limit of a RM-unstable flow, which is only approached in numerical simulations if the ambient fluid density behind the rear surface is extremely low. An accurate simulation of feedout requires much care to suppress the contribution of a numerically generated RM instability due to the ambient gas, which is not really there. The special case of feedout, on the other hand, turns out to be analytically tractable, so that explicit analytic formulas are now available for the time history of the areal mass perturbation amplitude, its early- and late-time asymptotics, oscillation frequency and time intervals characteristic of phase reversals. These formulas are shown to agree with our simulation results. Since the wavelengths characteristic of the inner surface roughness in laser pellets are $\sim 100\text{ }\mu\text{m}$ or more, and a typical thickness of the shock-compressed target is $50\text{ }\mu\text{m}$ or less, the dimensionless time interval τ_r relevant for feedout in laser fusion conditions does not exceed ~ 3 to 5 . Therefore, most of the relevant feedout processes occur before or within the first inverted peak of areal mass perturbation. Amplitude, timing and duration of this peak are given by our theory, which agrees with our simulations.

The available data on feedout perturbation growth obtained in indirect-² and direct-drive³ experiments agrees with the physical picture outlined in our paper. Much more remains to be done in experiment, however, in order to study the feedout process in full detail and ensure validation of the codes in the feedout regime. Our preliminary estimates indicate that such experiments are not beyond the reach of the existing laser facilities and diagnostic techniques.

Acknowledgements

The authors are grateful to Dr. Y. Aglitskiy for stimulating discussions of the available experimental opportunities. One of us (N. M.) wishes to thank Dr. S. P. Obenschain and Laser Plasma Branch at NRL for their support and hospitality during the performance of this research. This work was sponsored by the U.S. Department of Energy through the contract for the Naval Research Laboratory.

References

- ¹ R. Betti, V. Lobatchev, and R. L. McCrory, Phys. Rev. Lett. **81**, 5560 (1998).
- ² D. P. Smitherman, R. E. Chrien, N. M. Hoffman, and G. R. Magelssen, Phys. Plasmas **6**, 932 (1999).
- ³ K. Shigemori, M. Nakai, H. Azechi, K. Nishihara, R. Ishizaki, T. Nagaya, H. Nagatomo, and K. Mima, Phys. Rev. Lett. **84**, 5331 (2000).
- ⁴ K. O. Mikaelian, Phys. Rev. A **31**, 410 (1985).
- ⁵ A. L. Velikovich and L. Phillips, Phys. Fluids **8**, 1107 (1996).
- ⁶ Y. Yang, Q. Zhang, and D. H. Sharp, Phys. Fluids **6**, 1856 (1994).
- ⁷ A. L. Velikovich, Phys. Fluids **8**, 1666 (1996).
- ⁸ Y. Kivity and M. Hanin, Israel Journal of Technology **8**, 139 (1970); Phys. Fluids **24**, 1010 (1981).
- ⁹ A. L. Velikovich, J. P. Dahlburg, J. H. Gardner, and R. J. Taylor, Phys. Plasmas **5**, 1491 (1998).
- ¹⁰ K. O. Mikaelian, Phys. Rev. Lett. **71**, 2903 (1993); Phys. Fluids **6**, 356 (1994).
- ¹¹ K. A. Meyer and P. J. Blewett, Phys. Fluids **15**, 753 (1972).
- ¹² M. Vandenboomgaerde, C. M gler, and S. Gauthier, Phys. Rev. E **58**, 1874 (1998).
- ¹³ R. L. Holmes, G. Dimonte, B. Fryxell, M. L. Gittings, J. W. Grove, M. Schneider, D. H. Sharp, A. L. Velikovich, R. P. Weaver and Q. Zhang, J. Fluid Mech. **389**, 55 (1999).
- ¹⁴ J. P. Boris and D. L. Book, J. Comput. Phys. **11**, 38 (1973), also see Solution of the Continuity Equation by the Method of Flux-Corrected Transport, *Methods in Computational Physics*, v. 16 (Academic Press, New York, 1976), pp. 85-129.
- ¹⁵ N. Metzler, A. L. Velikovich, and J. H. Gardner, Phys. Plasmas **6**, 3283 (1999).

- ¹⁶ S. E. Bodner, D. Colombant, K. Gerber, R. H. Lehmberg, E. A. McLean, A. N. Mostovych, M. S. Pronko, C. J. Pawley, A. J. Schmitt, J. D. Sethian, V. Serlin, J. A. Stamper, C. A. Sullivan, J. P. Dahlburg, J. H. Gardner, Y. Chan, A. V. Deniz, J. Hardgrove, T. Lehecka, and M. Klapisch, *Phys. Plasmas* **3**, 2098 (1996).
- ¹⁷ A. L. Velikovich, J. P. Dahlburg, A. J. Schmitt, J. H. Gardner, L. Phillips, F. L. Cochran, Y. K. Chong, G. Dimonte, and N. Metzler, *Phys. Plasmas* **7**, 1662 (2000).
- ¹⁸ Y. Aglitskiy, T. Lehecka, S. Obenschain, S. Bodner, C. Pawley, K. Gerber, J. Sethian, C. M. Brown, J. Seely, U. Feldman, G. Holland, *Applied Optics* **37**, 5253 (1998)

Figure captions

Fig. 1. Formation of a rippled rarefaction wave in a feedout situation. (a) A planar shock wave \mathbf{S} driven by a constant force \mathbf{F} approaches the valleys of the rear surface ripples. Mass and shock velocities v_0 and D_0 are shown in laboratory reference frame. (b) A rippled rarefaction wave starts to form near the valleys. In the reference frame of shocked gas, its leading edge \mathbf{L} propagates to the left at local speed of sound, a_1 . Its trailing edge, the expansion front \mathbf{E} , propagates to the right at constant velocity u_e . (c) A fully formed rippled rarefaction wave approaches the front surface. Before its breakout, the ripple amplitudes at its leading and trailing edges, \mathbf{L} and \mathbf{E} , are constant in time.

Fig. 2. Time history of mass variation in a weak rarefaction wave at $M_1 = 0.9946$: exact [Eq. (19), solid line] and explicit approximate [Eq.(20), dotted line] results of linear theory normalized to $\rho_1 \delta x_l^*$.

Fig. 3. Time history of mass variation in a strong rarefaction wave at $M_1 = 0$. (a) Exact solution (22) and asymptotic solution (25) (solid and dotted lines, respectively) for $\gamma_1 = 5/3$. (b) Exact solutions (22) for γ_1 varied between $7/5$ and $9/5$. (c) Same for γ_1 varied between $5/2$ and 5 : no second phase reversal for $\gamma_1 > 2.82$.

Fig. 4. Time history of mass variation in a rarefaction waves at M_1 varied from 0 (thick solid line) to 0.8 (dashed line) with increment 0.2.

Fig. 5. Time history of mass perturbation growth in a RM unstable configuration: total mass variation δm and contributions to it from perturbations at the contact interface, δm_c , and in the reflected rarefaction wave, δm_r (solid, dashed, and dotted lines, respectively): (a) $\rho_2 / \rho_{01} = 10^{-1}$, Mach number of the reflected rarefaction wave

$M_1 = 0.75$; (b) $\rho_2 / \rho_{01} = 10^{-2}$, $M_1 = 0.53$; (c) $\rho_2 / \rho_{01} = 10^{-3}$, $M_1 = 0.36$; and (d) $\rho_2 / \rho_{01} = 10^{-4}$, $M_1 = 0.24$. Mass perturbation amplitude is normalized to its pre-interaction value, $(\rho_{01} - \rho_2)\delta x_0$.

Fig. 6. Displacement of the contact interface (in units of δx_0 , solid lines) and its time derivative (the growth rate, shown in units of $ku_t \delta x_0$, dashed lines) for (a) $\rho_2 / \rho_{01} = 10^{-3}$ and (b) $\rho_2 / \rho_{01} = 1.5 \cdot 10^{-4}$. Dashed straight lines show the asymptotic growth rates predicted by the MB and VMG prescriptions.

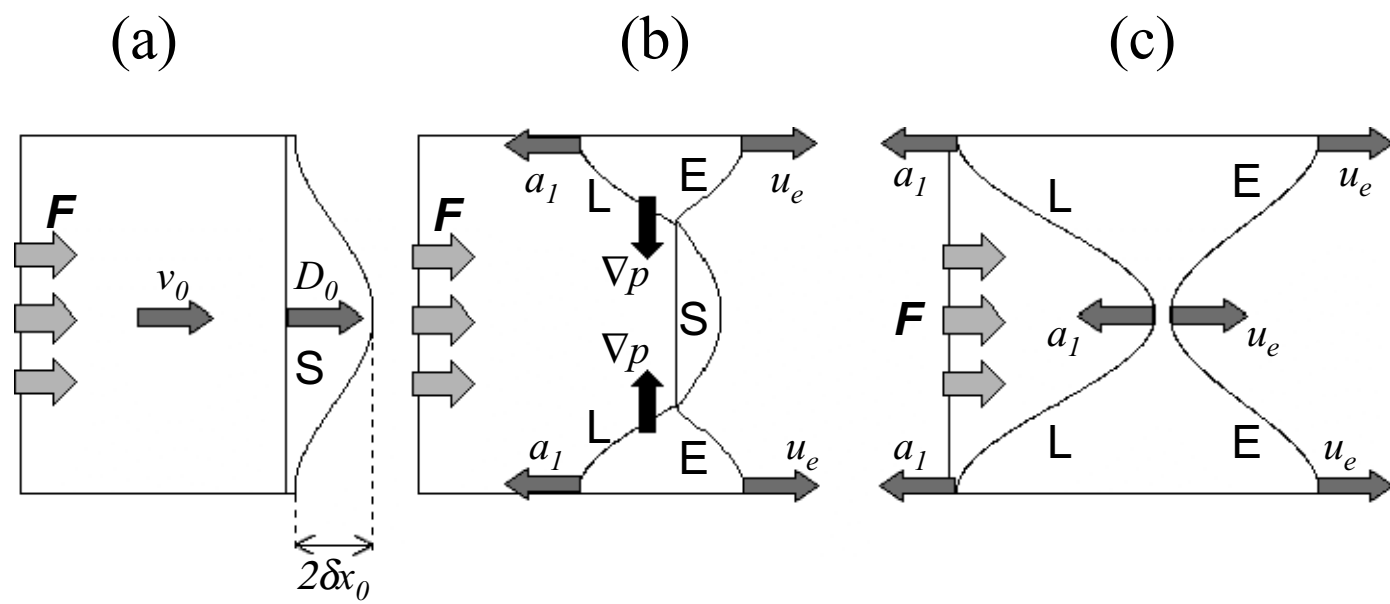
Fig. 7. Mass perturbation growth due to the RM instability at density ratio $\rho_2 / \rho_{01} = 0.1$. Solid line — numerical simulation, dotted line — analytical theory [same as solid line in Fig. 5(a)].

Fig. 8. Mass perturbation growth due to the RM instability at density ratio $\rho_2 / \rho_{01} = 10^{-3}$. Solid line — numerical simulation, dotted line — analytical theory [same as solid line in Fig. 5(c)], dashed line — analytical theory for the case of feedout [same as solid line in Fig. 3(a)].

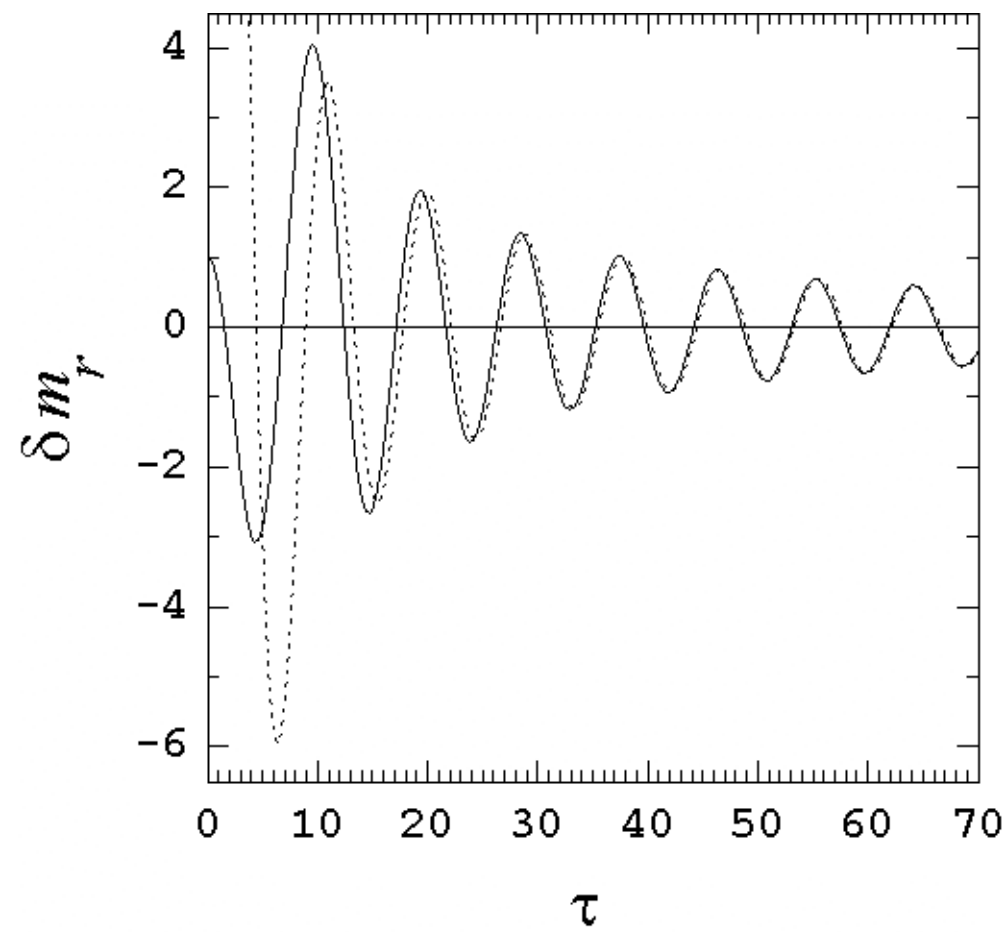
Fig. 9. Evolution of rms mass variation in a laser-driven 60- μm solid plastic target with initial ripple amplitude 1 μm , and varied ambient density behind its rippled rear surface [here ρ_{back} stands for $\rho_2 / (1.07 \text{ g/cm}^3)$].

Fig. 10. Laser pulse shape with intensity increased from a constant low-intensity foot to the main drive (a) and the corresponding evolution of rms mass variation in a 60- μm solid plastic target with initial ripple amplitude 1 μm , $\rho_2 / \rho_{01} = 10^{-3}$, and varied ripple wavelength (b).

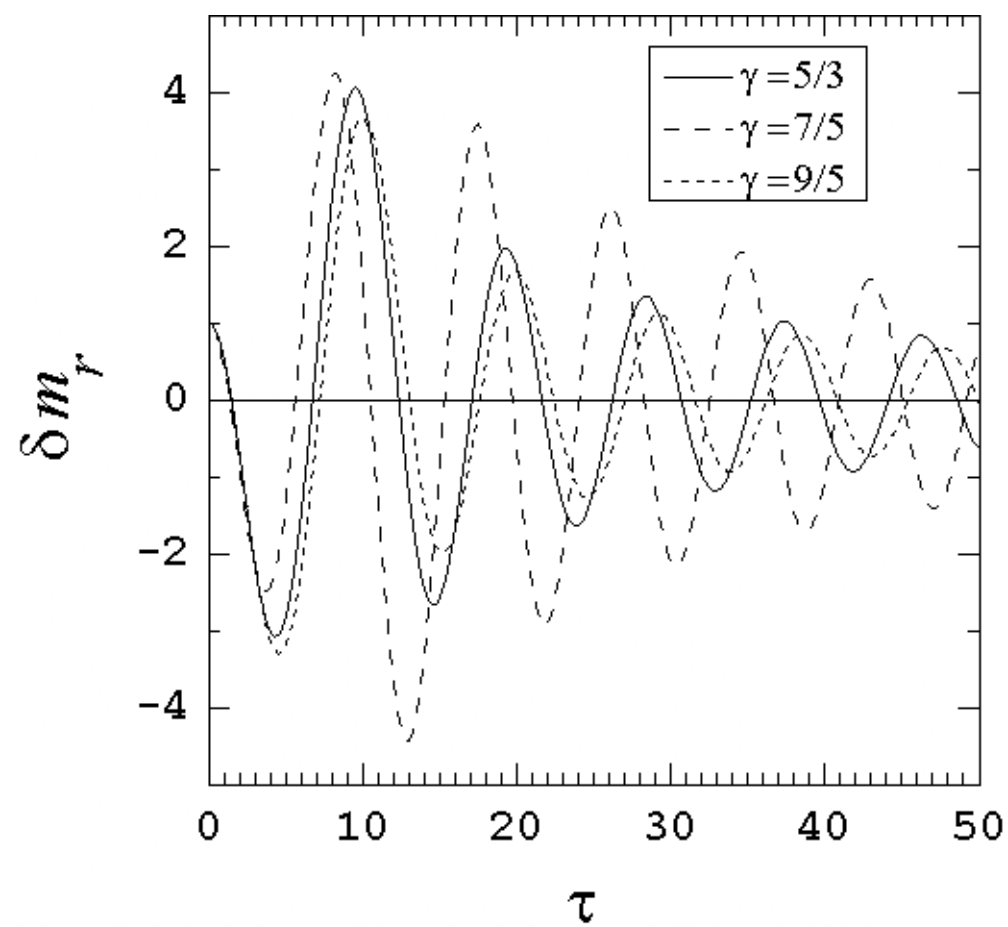
Fig. 11. Density contours for the case $\lambda = 30 \text{ } \mu\text{m}$ of Fig. 10, taken at $t = 0$ (a), 6.9 ns (b), 8.4 ns (c), and 9.6 ns (d).



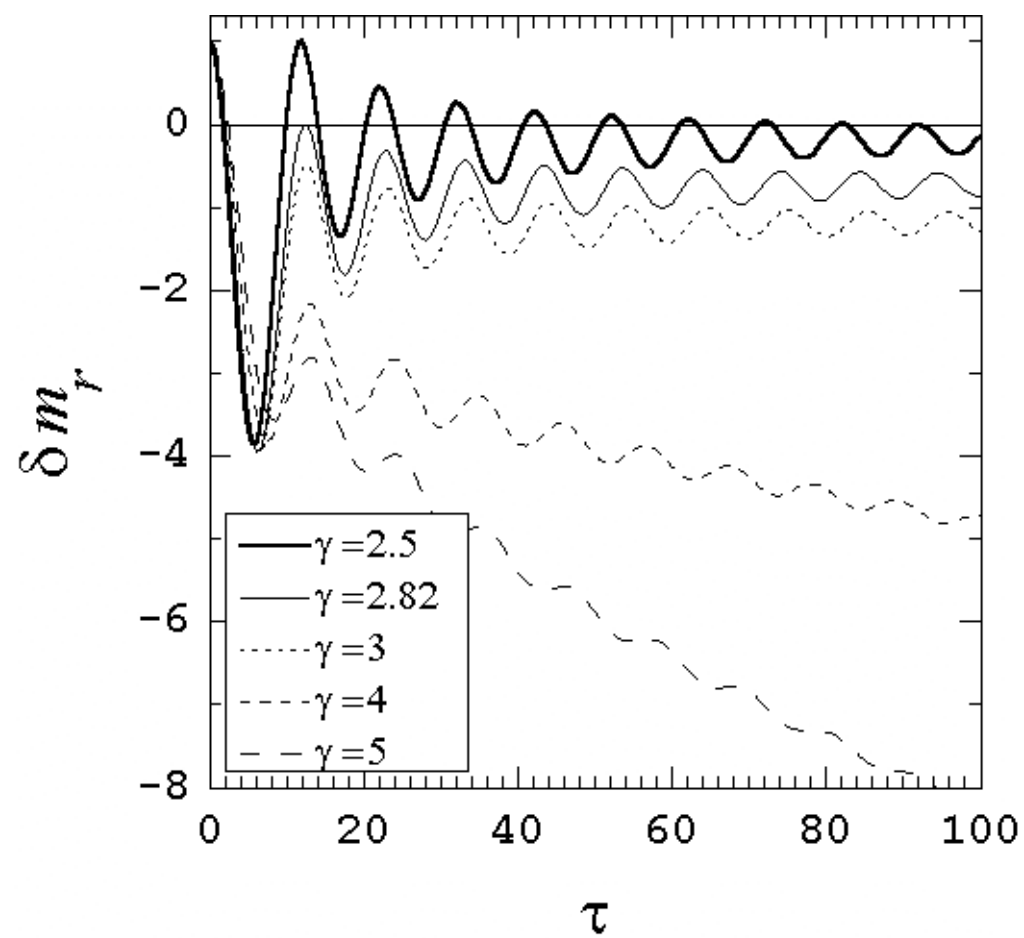
Velikovich et al., Fig. 1



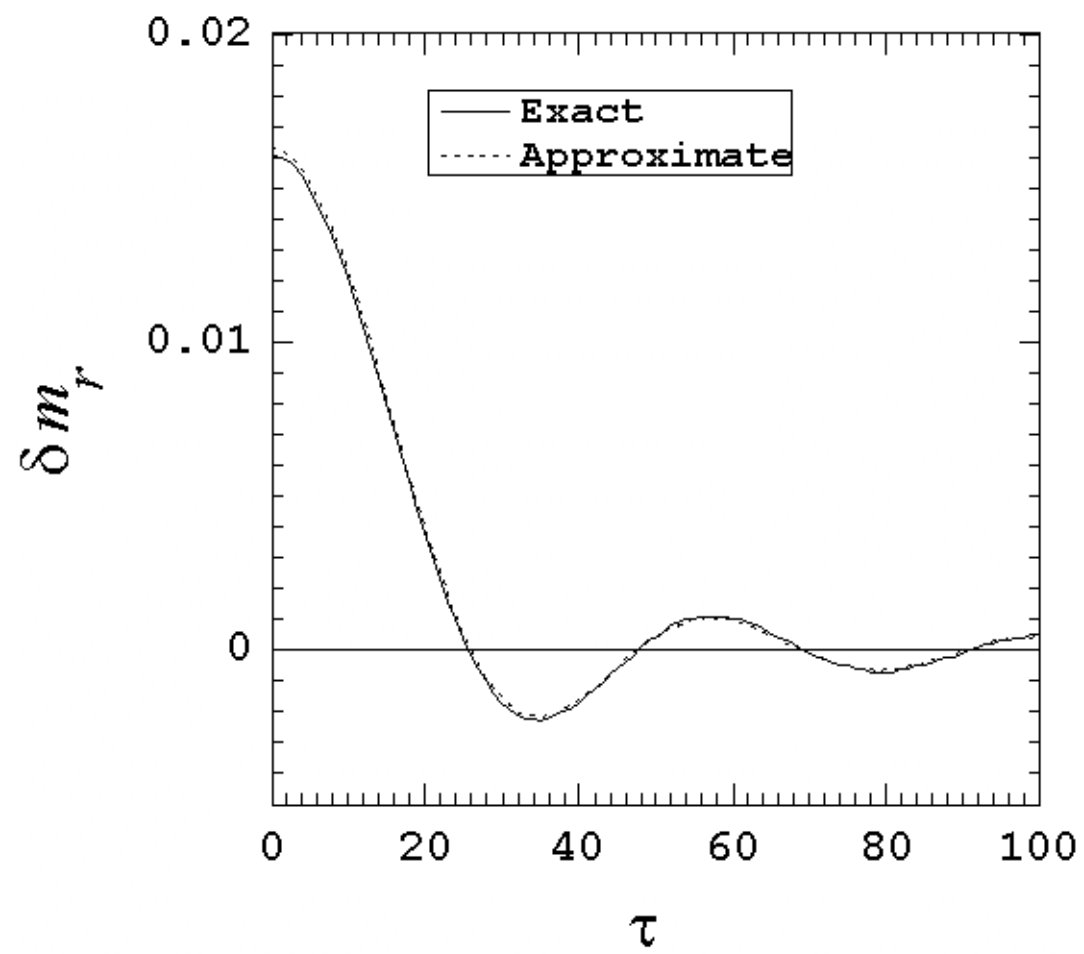
Velikovich et al., Fig. 3a



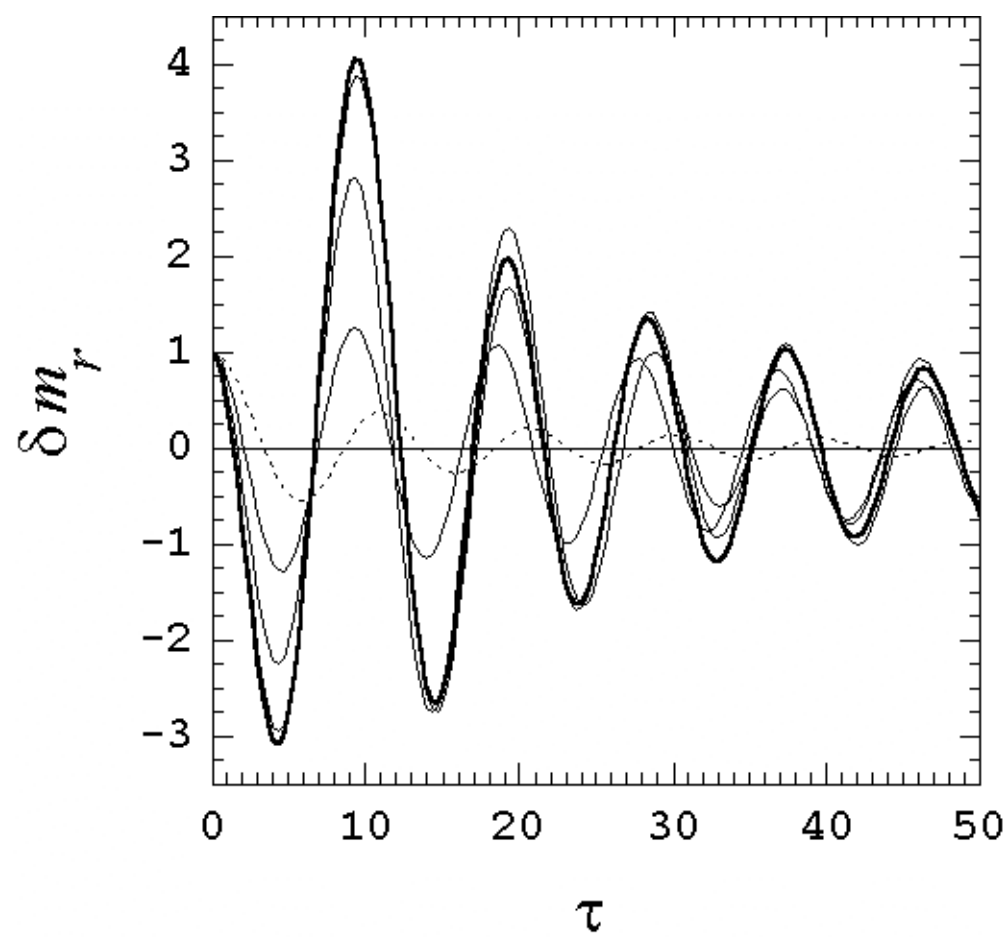
Velikovich et al., Fig. 3b



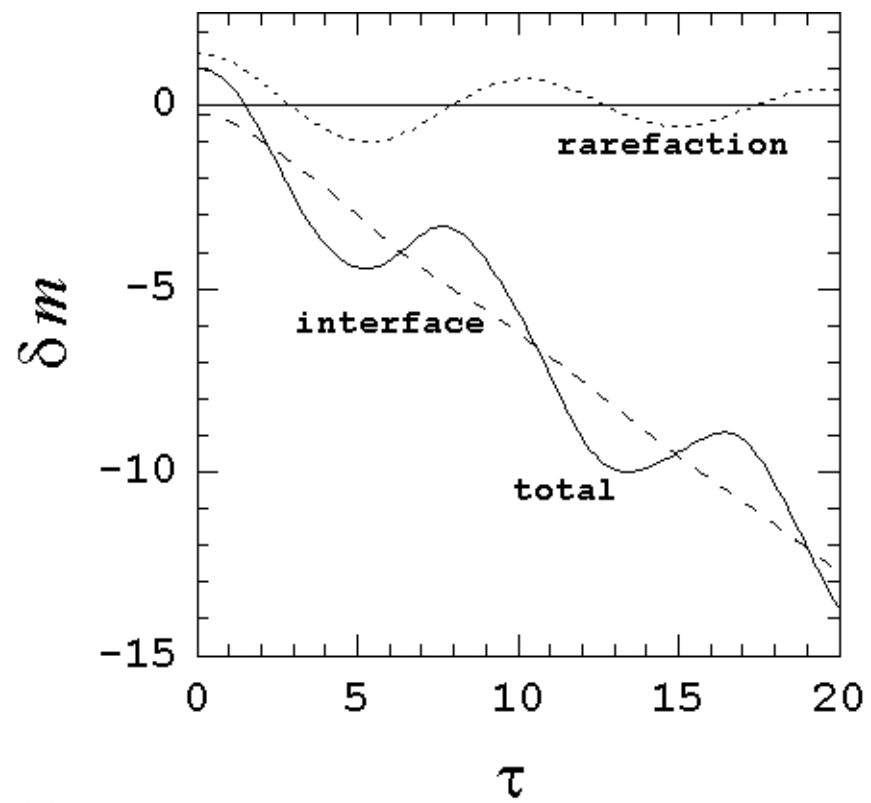
Velikovich et al., Fig. 3c



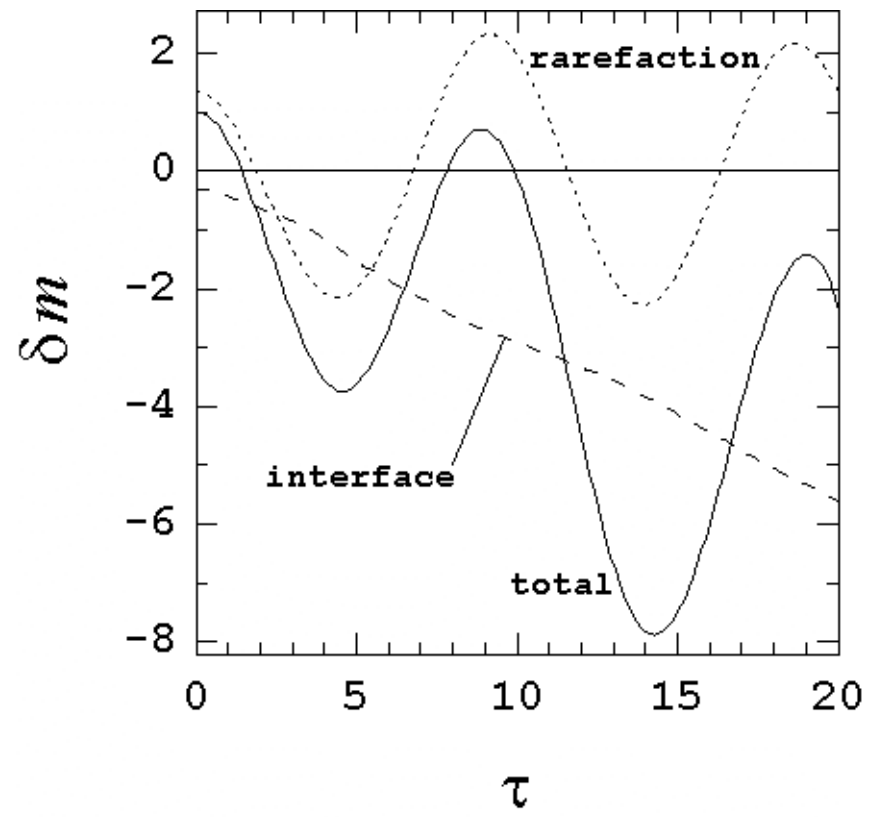
Velikovich et al., Fig. 2



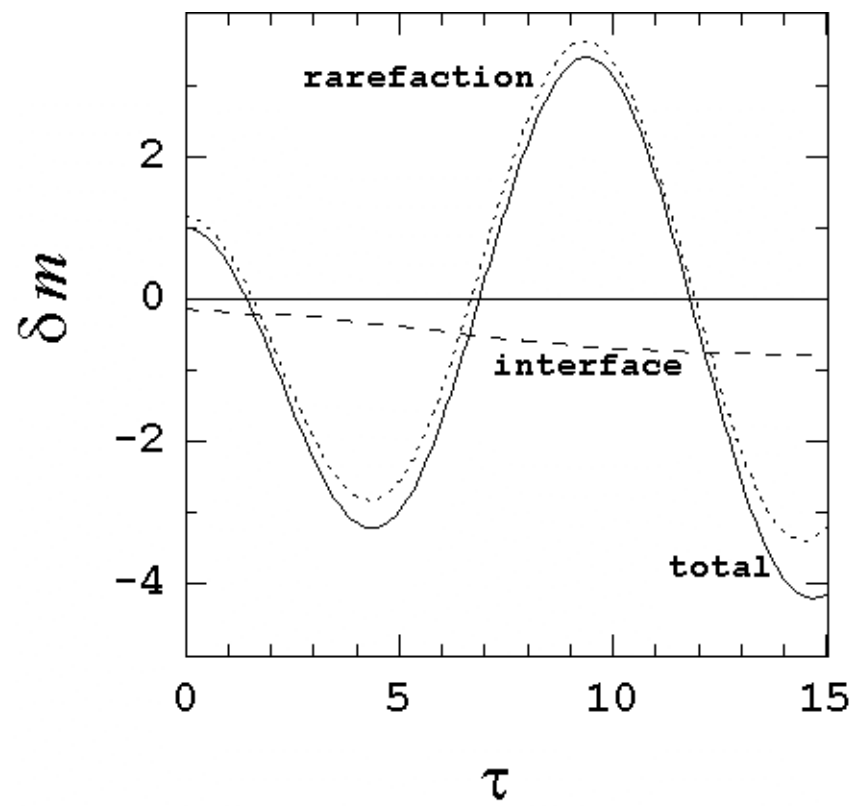
Velikovich et al., Fig. 4



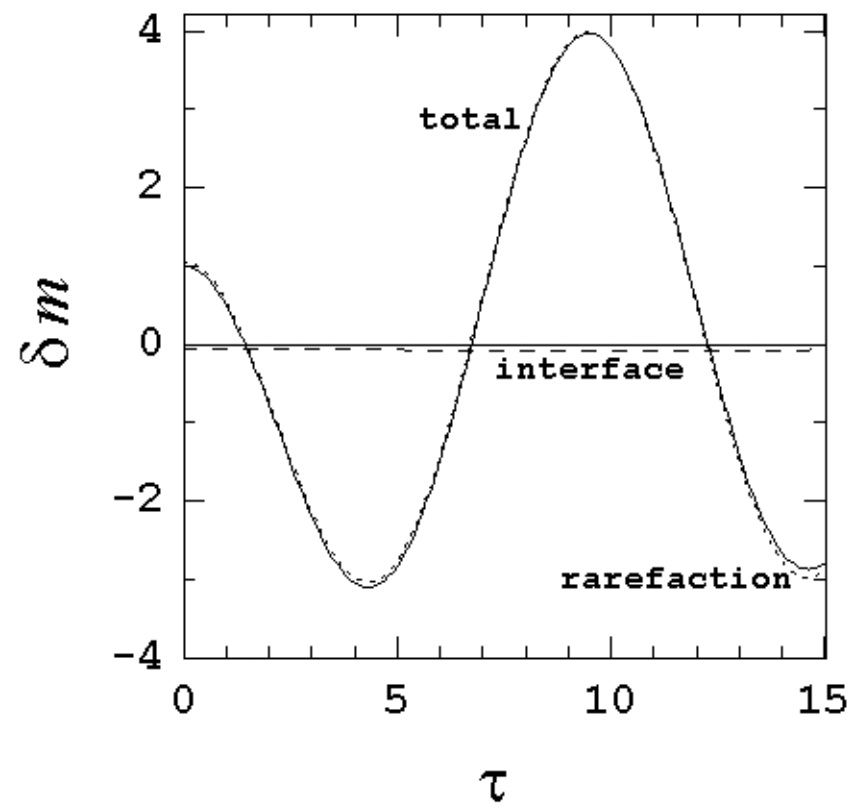
Velikovich et al., Fig. 5a



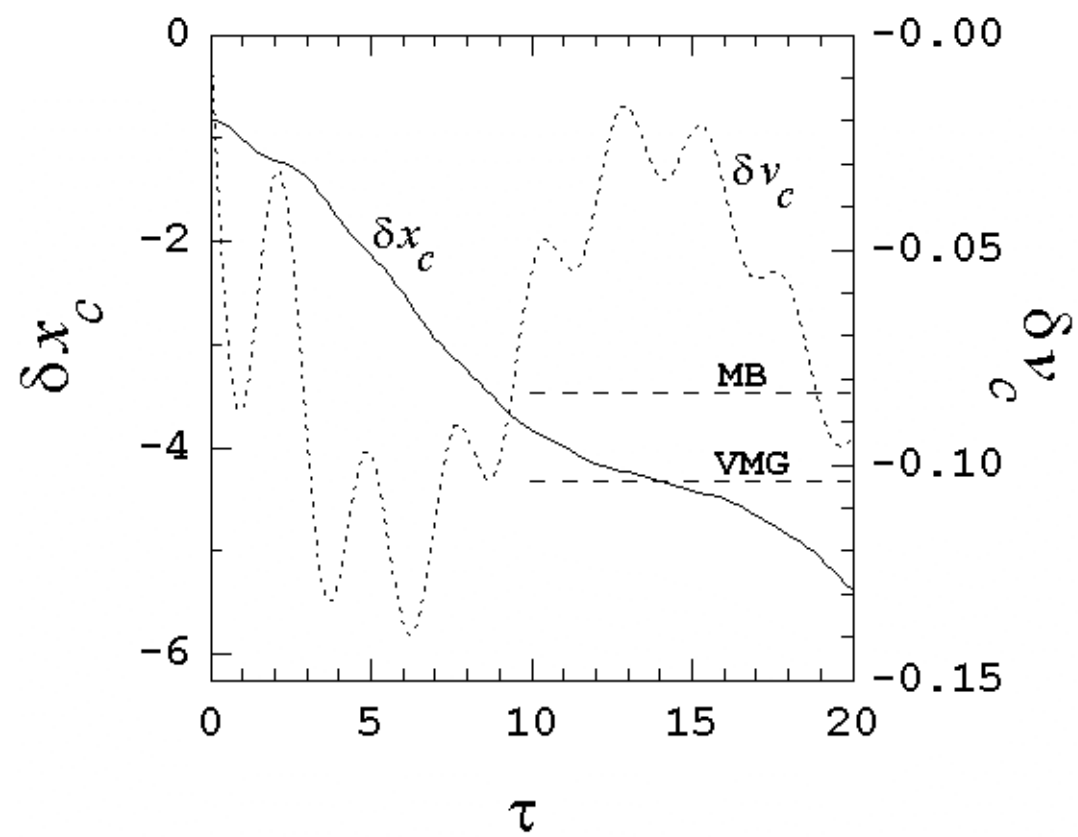
Velikovich et al., Fig. 5b



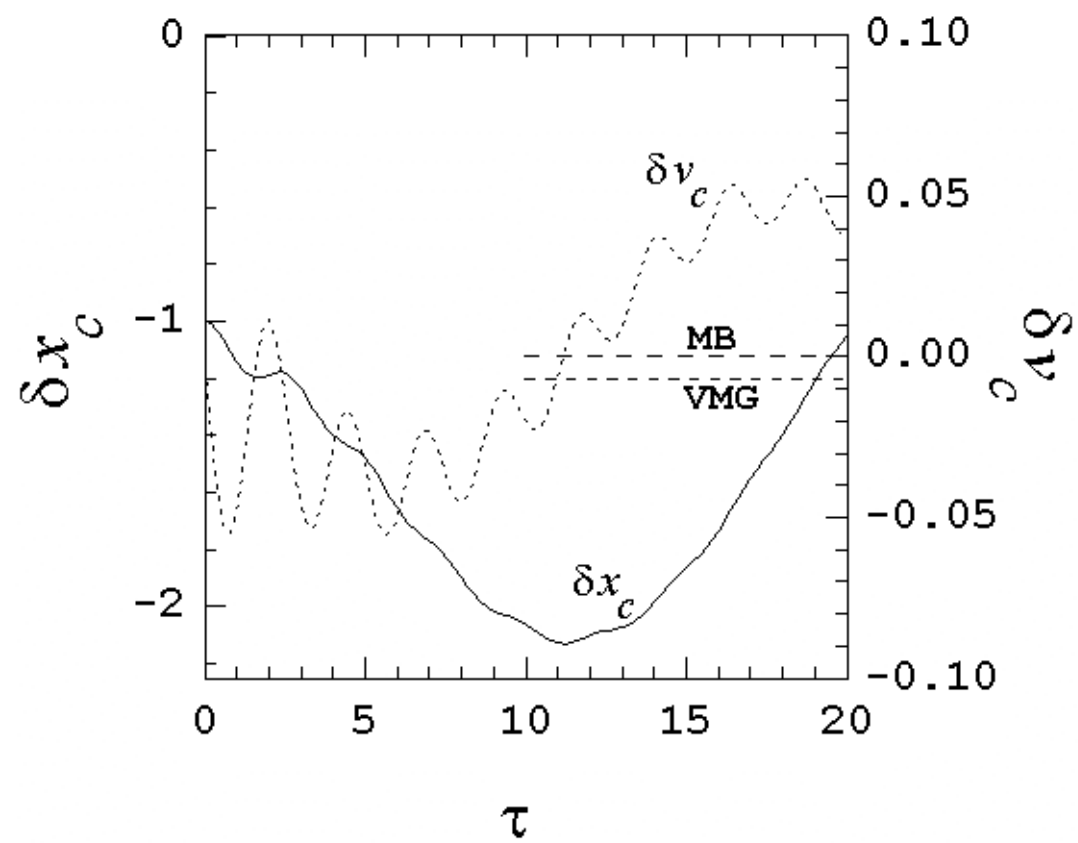
Velikovich et al., Fig. 5c



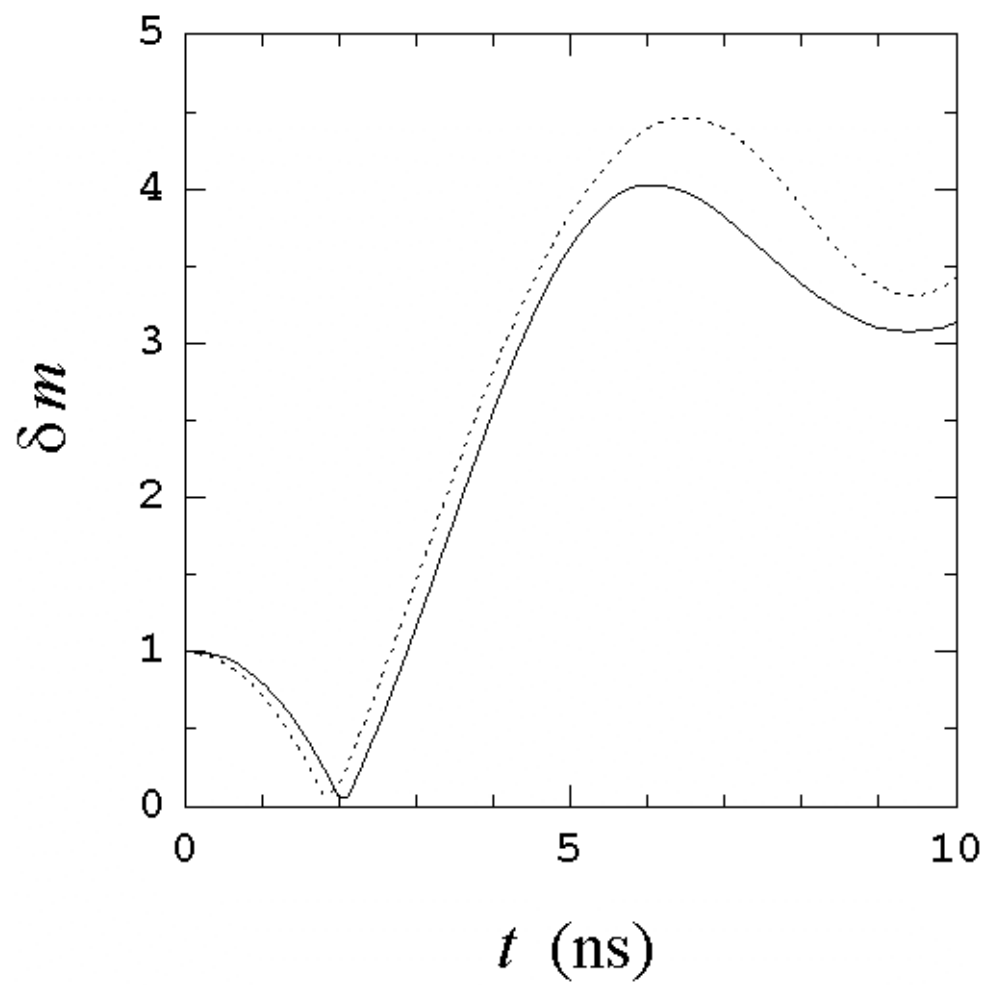
Velikovich et al., Fig. 5d



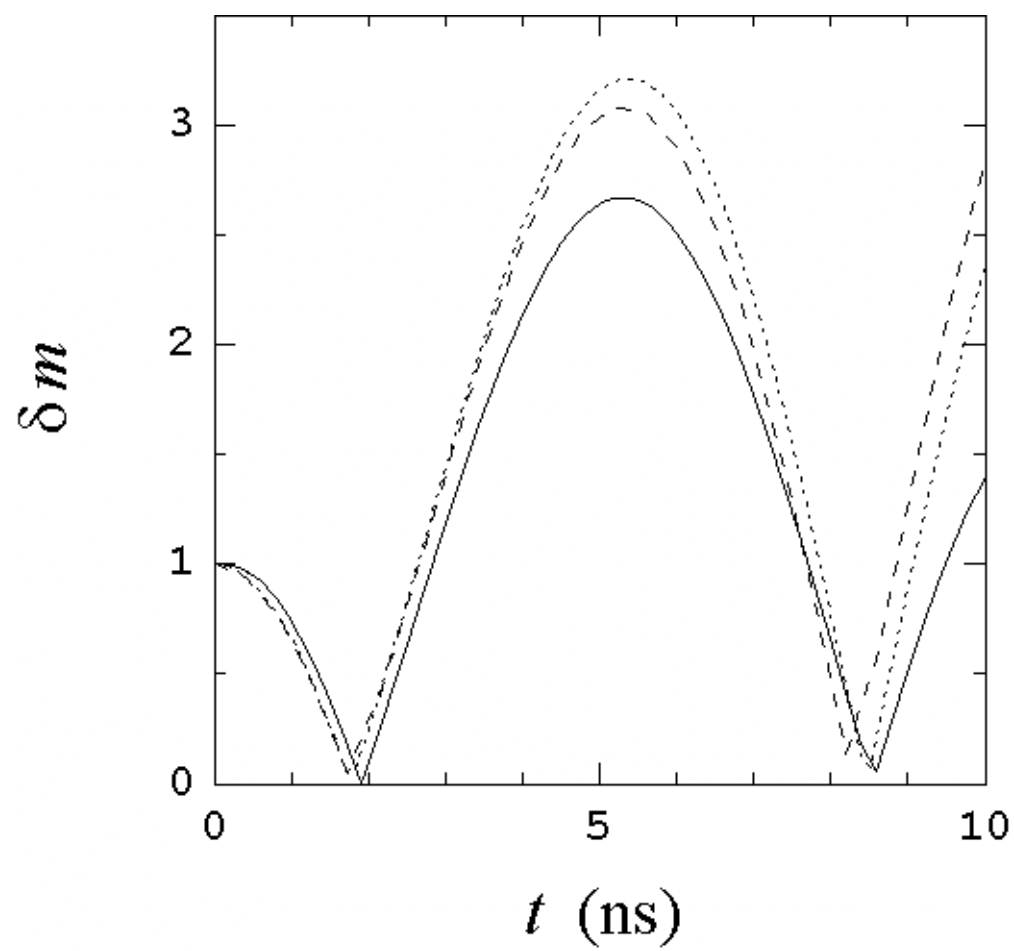
Velikovich et al., Fig. 6a



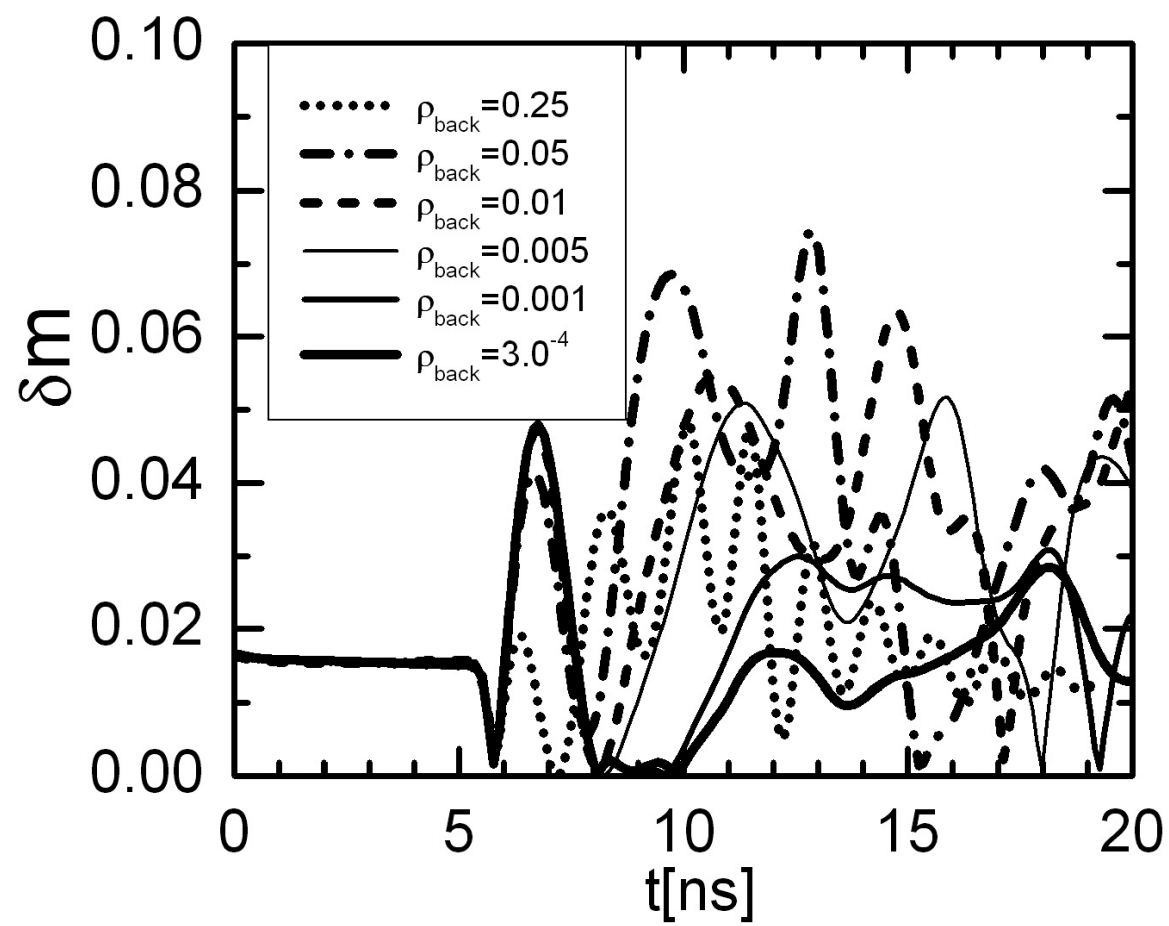
Velikovich et al., Fig. 6b



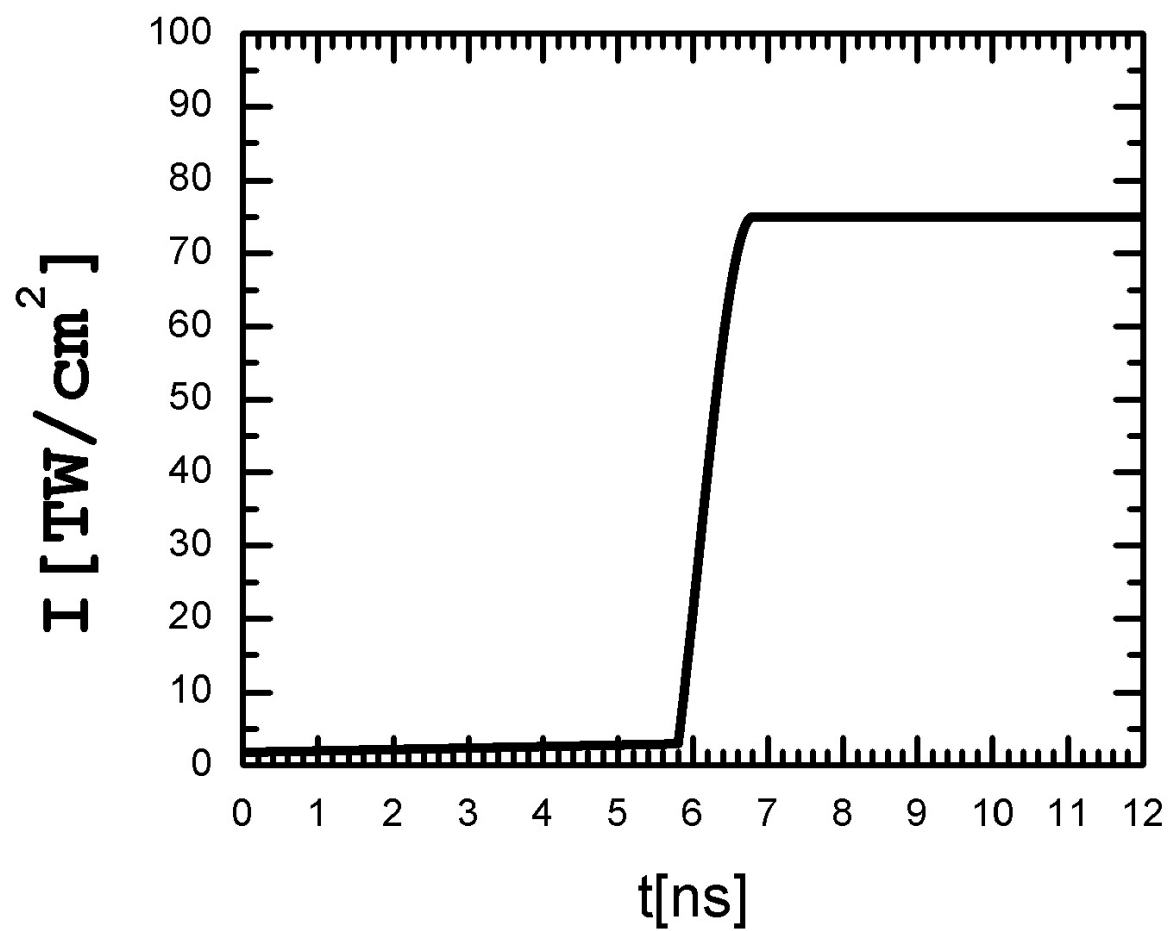
Velikovich et al., Fig. 7



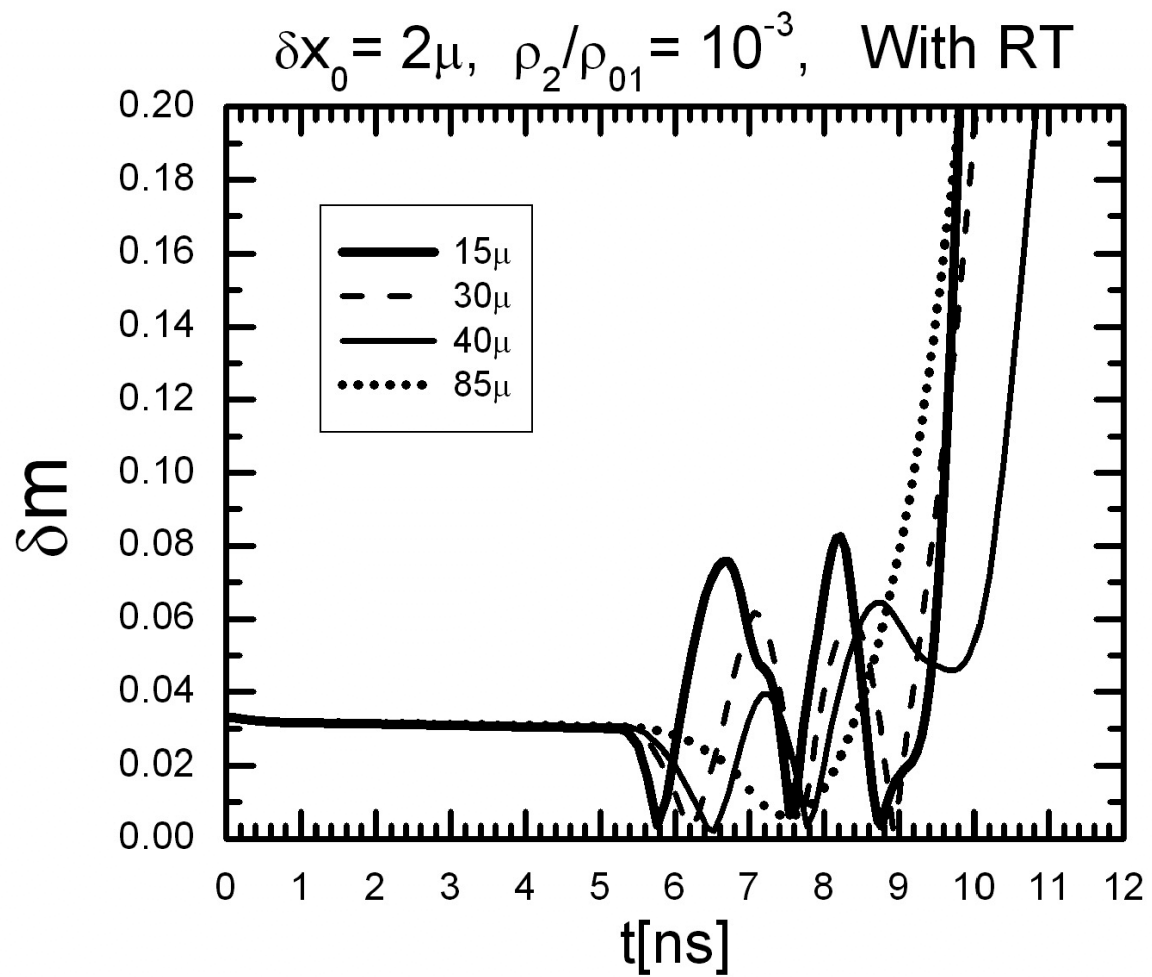
Velikovich et al., Fig. 8



Velikovich et al., Fig. 9

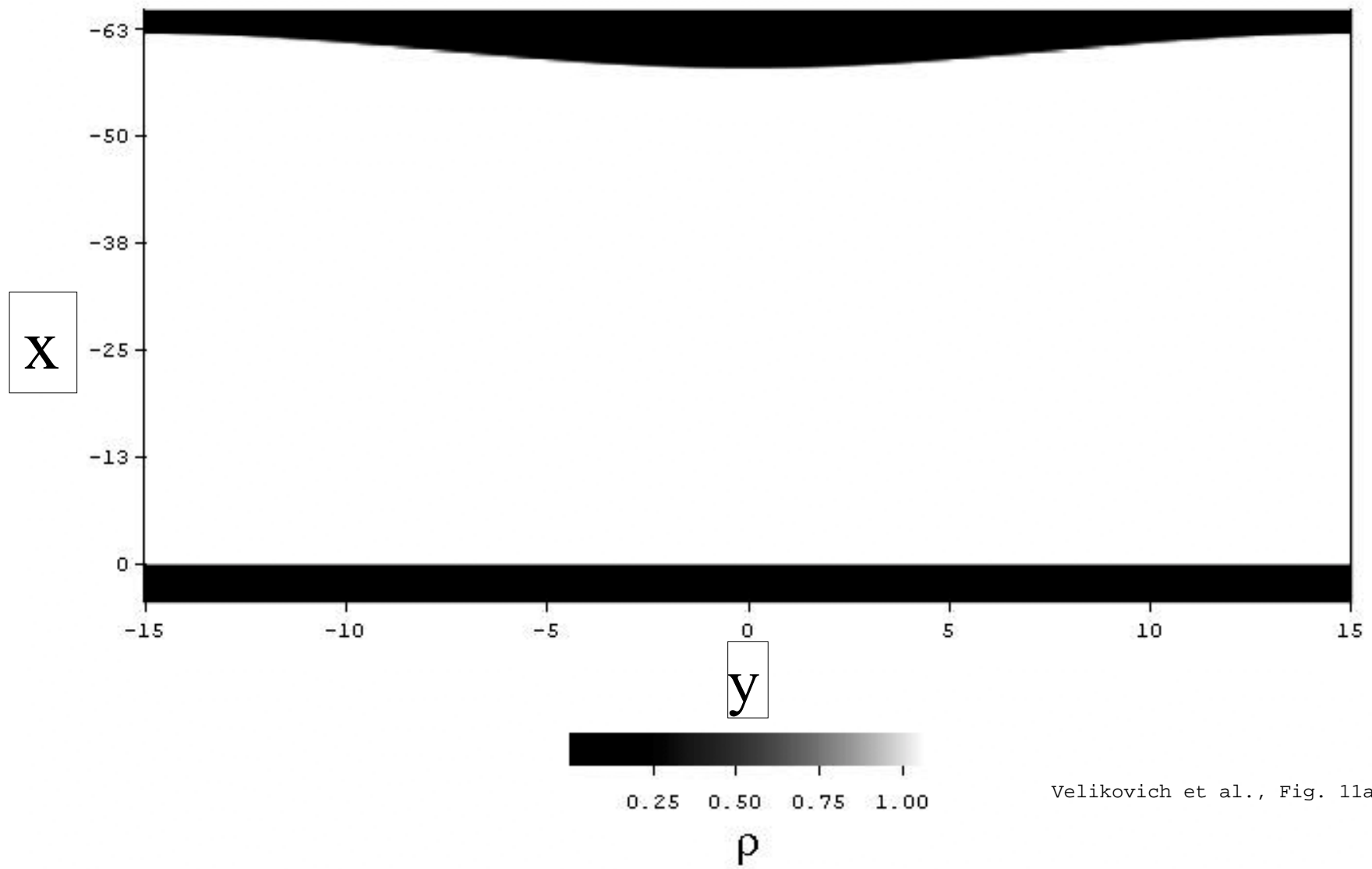


Velikovich et al., Fig. 10a



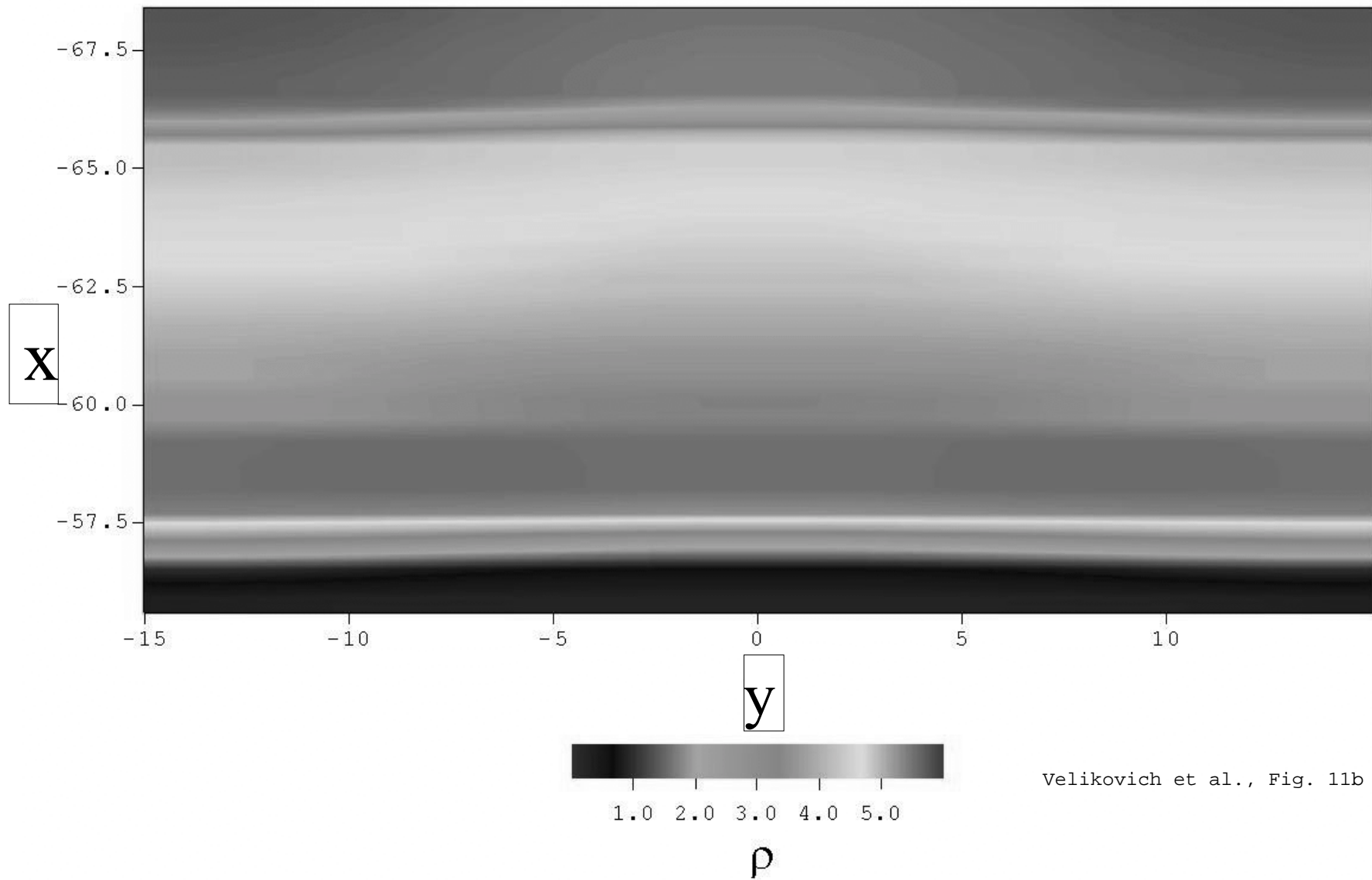
Velikovich et al., Fig. 10b

$$\lambda=30\mu, \quad \delta m=2\mu, \quad t=0\text{ns}$$



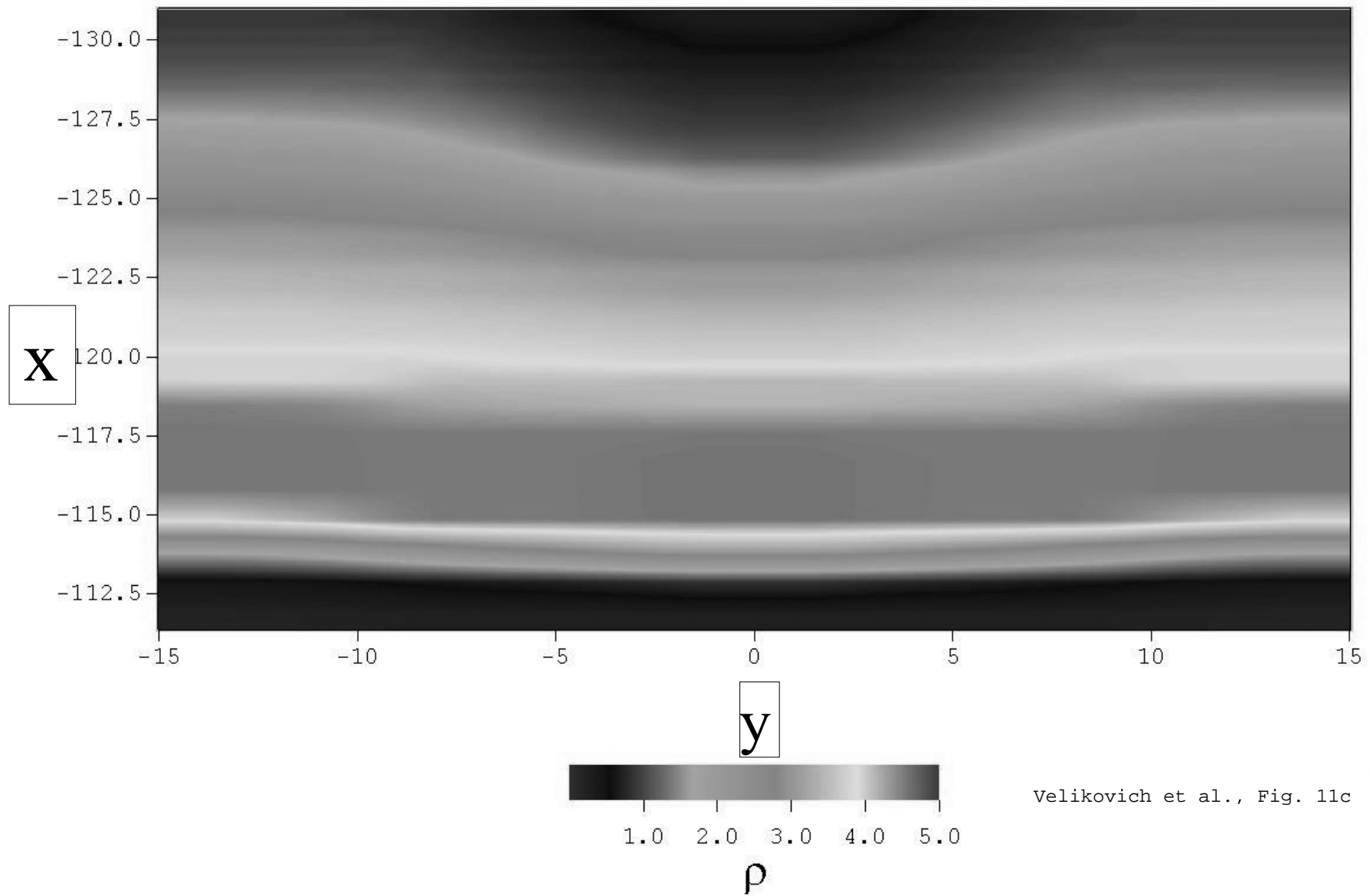
Velikovich et al., Fig. 11a

$$\lambda=30\mu, \quad \delta m=2\mu, \quad t=6.9\text{ns}$$

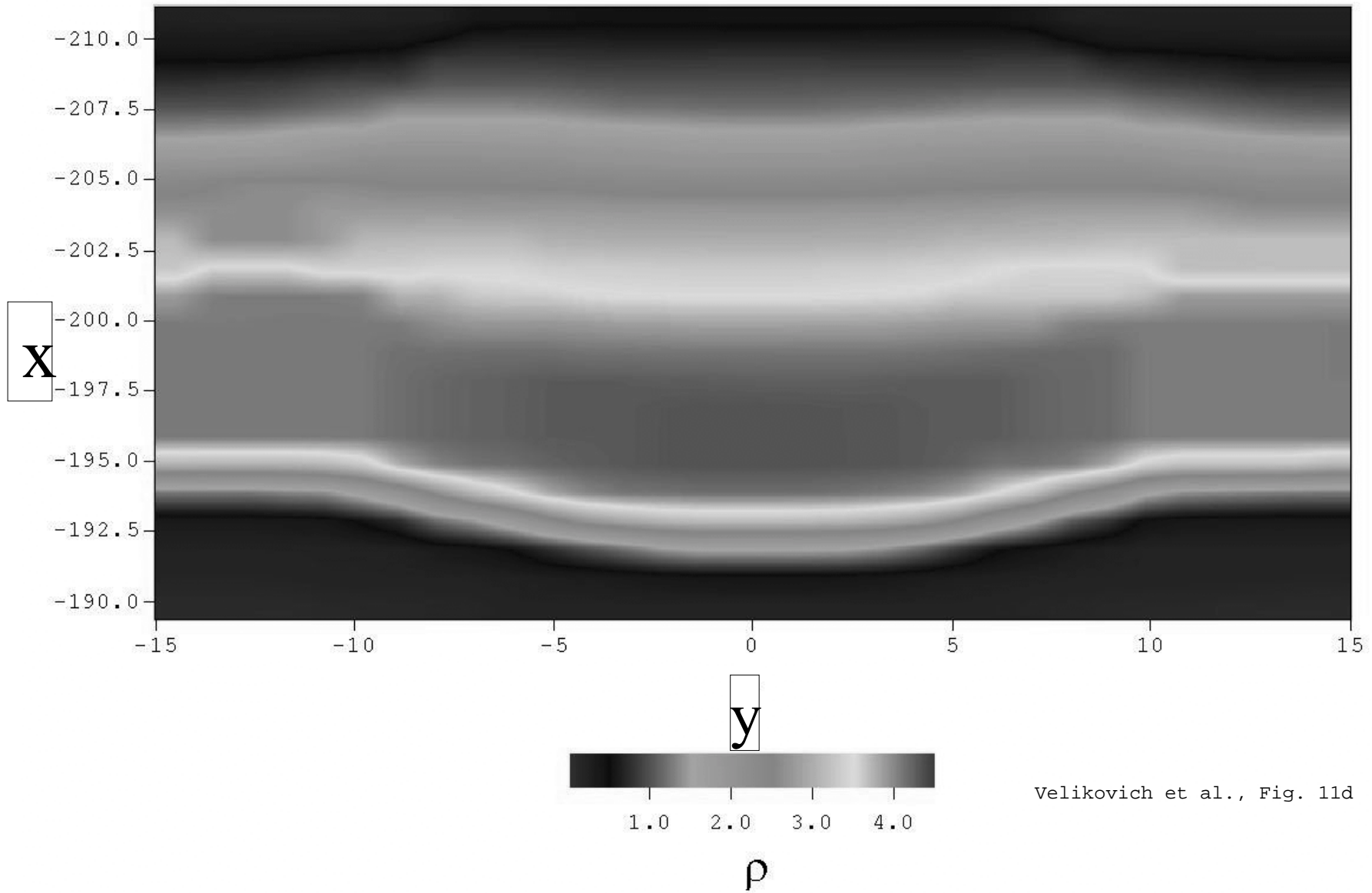


Velikovich et al., Fig. 11b

$$\lambda=30\mu, \quad \delta m=2\mu, \quad t=8.4\text{ns}$$



$$\lambda=30\mu, \quad \delta m=2\mu, \quad t=9.6\text{ns}$$



Velikovich et al., Fig. 11d